Journal of Geophysical Research: Oceans

RESEARCH ARTICLE
10.1029/2017JC013221

# Estimates of Surface and Subsurface Boundary Current Transport Around Australia

**Sarath Wijeratne[1], Charitha Pattiaratchi[1], and Roger Proctor[2]**

[1]Oceans Graduate School & The UWA Oceans Institute, The University of Western Australia, Crawley, WA, Australia, [2]Integrated Marine Observing System, University of Tasmania, Hobart, TAS, Australia

**Key Points:**
- Major inflows to the Leeuwin Current and Leeuwin Undercurrent are provided by the South Indian Counter Current
- The main inflow (65%) to the East Australian Current is through the northern branches of the South Equatorial Current
- All Australian boundary current transport was enhanced during the 2011–2013 La Niña

**Supporting Information:**
- Supporting Information S1

**Correspondence to:**
S. Wijeratne,
sarath.wijeratne@uwa.edu.au

**Citation:**
Wijeratne, S., Pattiaratchi, C., & Proctor, R. (2018). Estimates of surface and subsurface boundary current transport around Australia. *Journal of Geophysical Research: Oceans*, *123*, 3444–3466. https://doi.org/10.1029/2017JC013221

Received 29 JUN 2017
Accepted 12 APR 2018
Accepted article online 19 APR 2018
Published online 17 MAY 2018



**Abstract** A 15 year (2000–2014) simulation of the oceans around Australia, with the shelf-scale model ozROMS, was used to estimate the mean, seasonal, and interannual variability of the surface and subsurface boundary currents and associated inflows. The simulation clarified some previous points of uncertainty and provided new information previously unknown and this is listed here. In the Indian Ocean, flow through the Timor Passage was linked to southeast Australia through the Holloway (HLC), Leeuwin (LC), South Australian (SAC), and Zeehan (ZC) Currents. The main inflows were from the Indonesian Throughflow and Eastern Gyral Current in the north whilst the central and southern branches of the South Indian Counter Current (SICC) provided major (>60%) inflows to the LC in the west. The HLC at North-west Cape was at a maximum in April–May and its annual cycle accounted for 70% of the seasonal variance of LC, SAC, and ZC. In the Pacific Ocean, the northern branches of the South Equatorial Current were the main inputs to initiate the Hiri and East Australian (EAC) Currents flowing north and south, respectively, at ~15°S. Inflow from the South Caledonia Jet to the EAC was ~35%. The Flinders Current (FC) contributed to the Leeuwin Undercurrent (LU) directly as a northward flow and LU was enhanced from inflow from the subsurface southern SICC in the west (~32–33°S). The majority of LU flowed westward offshore between 24 and 29°S while ~25% continued northward to the northwest shelf. All Australian surface boundary currents systems were enhanced during the 2011–2013 La Niña.

## 1. Introduction

Australia is an island continent surrounded by surface and subsurface boundary currents that flow along the continental shelf/slope as components of the subtropical gyre circulation in the South Indian and South Pacific oceans. These boundary currents are enhanced through inflows from the ocean basins and are an important conduit for the poleward heat and mass transport along the east and west coasts, and for inter-ocean water exchange in the tropics, as part of the Indonesian Throughflow (Sen Gupta et al., 2016; Sprintall et al., 2009), and the subtropics, from the Tasman outflow (Hu et al., 2015; Ridgway & Godfrey, 1994; van Sebille et al., 2012). Major surface boundary currents include (Figure 1a): Indonesian Throughflow (ITF), Holloway (HLC), Leeuwin (LC), South Australian (SAC), Flinders (FC), Zeehan (ZC), East Australian (EAC), and Hiri (HC) currents. The major subsurface currents (excluding the surface currents that extend to depths >300 m) include (Figure 1b): Tasman Outflow (TO) and the Leeuwin Undercurrent (LU).

The ITF provides a tropical connection between the Pacific and Indian Oceans, with its main pathway westward located along the northern Australian coastline through the Timor Passage (TP) (Gordon & McClean, 1999). Recent observation-based estimates of the ITF originating from the TP suggest an annual mean of 7.5 Sv, which comprises 50% of the total ITF (~15 Sv) to the Indian Ocean (Sprintall et al., 2009). The ITF contributes to the South Equatorial Current (SEC), the major westward flow across the Indian Ocean to the eastern Indian Ocean. A portion of the SEC returns eastward as the South Indian Counter Current (SICC) (Lambert et al., 2016; Menezes et al., 2013, 2014, 2016). Part of the SEC recirculates eastward as the Eastern Gyre (EG). Wind stress curl and strong salinity gradients in the southeastern Indian Ocean have been attributed to the EG formation (Menezes et al., 2013). The Eastern Gyral Current (EGC) flows eastward on the southern flank of the tropical EG fed by a partial retroflection of the SEC and inflows from northern SICC (Menezes et al., 2014, 2016). A review of the literature, however, finds inconsistent EGC pathways, direction, and eastward extent with the many studies defining EGC inflow at North West Cape (De Deckker et al., 2012; Domingues et al., 2007; Feng et al., 2003; Meyers et al., 1995; Waite et al., 2007).

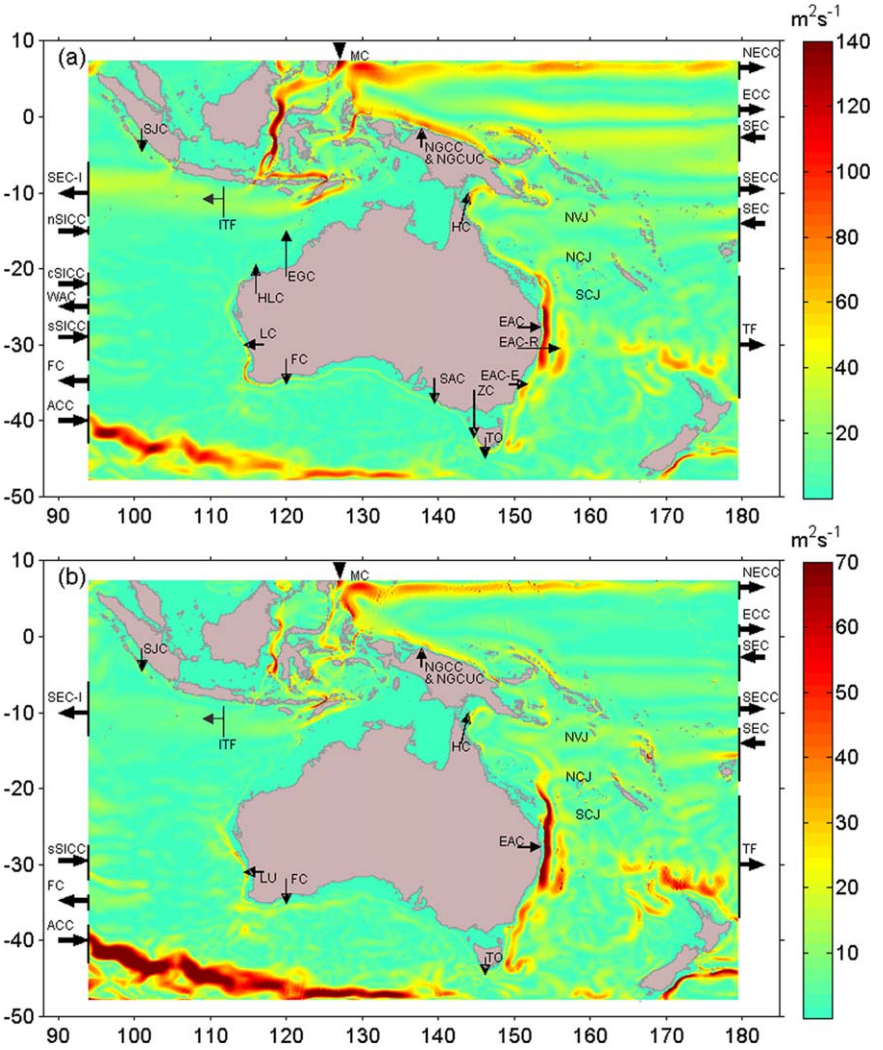


**Figure 1.** The ozROMS model domain covering the entire Australian shelf, slopes, and adjacent Deep Ocean. The model estimated mean vertically integrated currents between: (a) 0 and 300 m depth; and, (b) 300 m and 1,000 m depth. The mean values are from the entire simulation period (2000–2014). The major current systems discussed in this paper are; ITF = Indonesian throughflow; SEC-I = South equatorial current, Indian Ocean; EGC = East Gyral Current; HLC = Holloway Current; LC = Leeuwin Current; LU = Leeuwin Undercurrent; SICC = South Indian Counter Current (s: south, c: central; and, n:north); ACC = Antarctic Circumpolar Current; WAC = Western Australian Current; FC= Flinders Current; SAC = South Australian Current; EAC = East Australian Current; EAC-R = East Australian Current Recirculation; EAC-E = East Australian Current Extension; TF = Tasman Front; TO = Tasman Outflow; NVJ = North Vanuatu Jet; NCJ = North Caledonia Jet; SCJ = South Caledonia Jet; HC = Hiri Current; SCJ = South Java Current; ECC = Equatorial Counter Current; SECC = South Equatorial Counter Current; NECC = North Equatorial Counter Current; MC = Mindanao Current and NGCC/NGCUC = New Guinea Coastal Current/New Guinea Coastal Under Current.

A portion of the ITF-TP flows onto the north-western Australian continental shelf/slope as the HLC (Bahmanpour et al., 2016) and contributes to the unique poleward eastern boundary current along the west and south coasts, the LC (Pattiaratchi & Woo, 2009; Ridgway & Godfrey, 2015; Smith et al., 1991). The LC follows the curvature of the coastline and turns eastward at Cape Leeuwin (geographic locations are shown in Figure 2) and extends along the southern continental shelf/slope as the SAC. The LC/SAC becomes the ZC and flows around southern Tasmania (Baines et al., 1983; Cresswell, 2000).

In the Pacific Ocean, the westward flowing South Equatorial Current (SEC) impinges on the eastern continental shelf slope of Australia. The northern branches of the SEC (North Vanuatu Jet and North Caledonia Jet, Figure 1) bifurcate at ~15°S to initiate the HC, a clockwise circulation that flows into the Gulf of Papua (Figure 2) and the southward flowing EAC along the Australian coast (Godfrey et al., 1980). The EAC

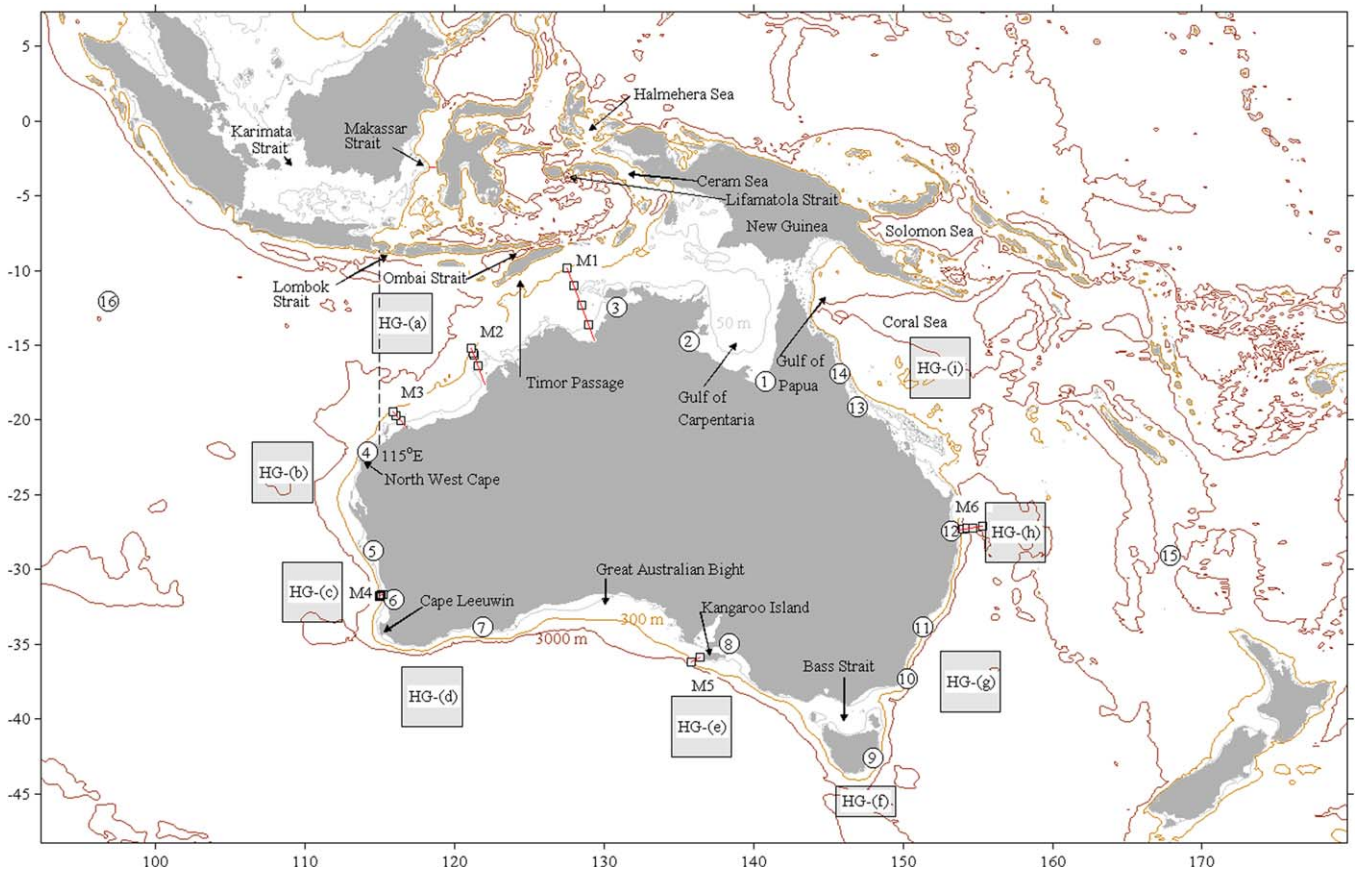


**Figure 2.** Model domain showing bathymetry and locations of model validation points/transects. The observational data used for model validation are denoted in circles for selected tide gauge sites: (1) Karumba; (2) Groote Eylandt; (3) Darwin; (4) Exmouth; (5) Geraldton; (6) Fremantle; (7) Esperance; (8) Port Adelaide; (9) Spring Bay; (10) Eden; (11) Sydney; (12) Brisbane; (13) Townsville; (14) Cairns; (14); (15) Norfolk Island; and, (16) Cocos Island. Current meter moorings sections are shown as squares: (M1) ITF shelf; (M2) Kimberly; (M3) Pilbara; (M4) Two Rocks; (M5) South Australia; and (M6) EAC (27°S section). The locations of ARGO profile data used to compare model results (Figure 5) are denoted in grey shaded squares names HG.

recirculation is defined as the northwards flow located further offshore of the main southward EAC flow (Zilberman et al., 2014). The main EAC flow separates from the Australian coast at latitudes 30°S–34°S and flows eastward as the Tasman Front (TF) (Bowen et al., 2005; Cetina-Heredia et al., 2014).

A part of the EAC, known as the EAC extension, reaches southern Tasmania and flows westward into the eastern Indian Ocean as the TO or Tasman Leakage (Ridgway & Dunn, 2007; van Sebille et al., 2012). The FC flows from east to west along Australia's southern shelves (Middleton & Bye, 2007) where it becomes a surface current offshore and an undercurrent along the continental shelf/slope beneath the LC (Furue et al., 2017). At Cape Leeuwin, the FC bifurcates with one arm flowing into the south-east Indian Ocean and the other moving northward as the LU.

Magnitudes of the transport, temporal, and spatial variability of the major surface boundary currents (e.g., LC, SAC, EAC, and FC) are generally known but details of inflows into these surface current systems and the transport and variability of the subsurface current systems are largely uncertain. It is known that both the LC and EAC strengthen as they flow southward along the western and eastern shelf slopes of Australia with inflows from the subtropical branches of SICC and SEC, respectively (Domingues et al., 2007; Ridgway et al., 2008), however a recent study by Yit Sen Bull and van Sebille (2016) suggested that tropical sources account for between 60 and 78% of the LC transport.

The numerical model ozROMS, the first 3-dimensional shelf-scale model for all of Australia, was developed to investigate the circulation around Australia at sufficiently high spatial resolution to better resolve the continental shelf and slope processes. ozROMS includes forcing from astronomical tides and associated

barotropic and baroclinic mixing processes. This is in contrast to global models that are available for the region with spatial resolution of ~10 km and do not include tidal forcing. Many of the continental shelf regions around the Australian continent have relatively narrow continental shelves (<80 km) and relatively steep continental slopes. These features are not well resolved in 10 km resolution models with only a few grid points across the shelf and inherent smoothing of the continental slopes. It is also important to note that the northwest shelf of Australia experiences a 10 m tidal range; through the inclusion of tidal forcing ozROMS is able to resolve the low-frequency transport variability against a background of nonlinear tidal rectification and mixing (Glorioso & Simpson, 1994). The importance of tidal and internal tidal mixing on cross-shelf and along-shelf slope transport has also been demonstrated by numerous previous studies (e.g., Castelao et al., 2010; Wang et al., 2013).

The focus of this paper is on describing and quantifying in greater detail than previous studies the mean and seasonal variability in the volume transport and inflows to surface and subsurface boundary currents along the entire Australian continental shelf and slope regions and the adjacent deep ocean (Figure 1).

## 2. Model Description and Validation

### 2.1. Model Description

The numerical model utilized here is the Regional Ocean Modelling System, ROMS (http://www.myroms.org) (Haidvogel et al., 2008), run in hindcast mode without data assimilation. The model domain was selected to allow the simulation of the major offshore flows that directly contribute to surface and subsurface boundary currents flowing along the continental shelf/slopes around Australia (Figures 1 and 2). ozROMS was nested within the global model HYCOM (Chassignet et al., 2007). Open boundaries in ozROMS were aligned to the HYCOM grid. The northern edge of the model domain was aligned to 7.4°N to capture the Mindanao current and was located in the eastward flow of the North Pacific counter current. The southern edge was aligned to 49°S and selected to capture the northern section of the Antarctic Circumpolar Current. Western and eastern boundaries were set to 92°E and 180°E, respectively, to include the Indian and Pacific Ocean basin inflows/outflows (SICC, SEC, TF etc.).

Bathymetry was derived from the GEBCO 30 arc-second gridded bathymetry (http://www.gebco.net/data_and_products/gridded_bathymetry_data/) and enhanced by additional data for the Australian region (Webster & Petkovic, 2005). The model horizontal grid spacing of 3–4 km (2,160 × 2,160 grid points) was chosen to allow as much topographic detail as possible and to resolve the major mesoscale eddy structures apparent in the boundary currents. The model vertical resolution comprised of 30 s-levels where the grid transformation and stretching parameters were chosen to define higher resolution near the surface and bottom boundaries in order to better resolve ocean boundary layers. The bathymetry was smoothed to minimize horizontal pressure gradient (HPG) errors through the following procedure: (1) the original bathymetry was smoothed using a Gaussian filter with a width twice the size of each raw data point; (2) smoothing was performed on the whole computational grid, where depths were <3,000 m.; (3) "spikes" in depths >3,000 m were removed; and, (4) the model domain was divided into several subregions and the bathymetry was smoothed in each sub region using a smooth positive method (Sikiric et al., 2009).

Atmospheric forcing (surface wind stress, sea level pressure, heat and freshwater fluxes) were obtained from 3 hourly, 0.125° horizontal resolution data from the European Centre for Medium-range Weather Forecasting (ECMWF) Interim archive. The open boundary salinity, temperature, transport (barotropic and 3-D velocity components), and mean sea levels were prescribed from the 1/12° daily HYCOM (Hybrid Coordinate Ocean Model) data. A combination of nudging and radiation conditions was used for the open boundary conditions. A sponge layer was also used adjacent to each open boundary where the horizontal eddy viscosity was increased linearly from 20 $m^2\ s^{-1}$ in the interior to 300 $m^2\ s^{-1}$ at the boundary over a distance of ~180 km (60 grid points). The "nudging" boundary zone had the same dimensions as the sponge layer, where the ozROMS model variables were nudged towards the daily mean HYCOM data.

The model open boundary tidal constituents were obtained from the Oregon State University (OSU) TPX07.2 global tidal model (http://volkov.oce.orst.edu/tides/global.html) with 13 tidal constituents defined: eight primary ($M_2$, $S_2$, $N_2$, $K_2$, $K_1$, $O_1$, $P_1$, $Q_1$); two long period ($M_f$, $M_m$), and three nonlinear ($M_4$, $MS_4$, $MN_4$). These harmonics were input to ozROMS open boundaries using the Chapman condition (Chapman, 1985) for elevation and the Flather condition (Flather, 1976) for depth-averaged current ellipses.

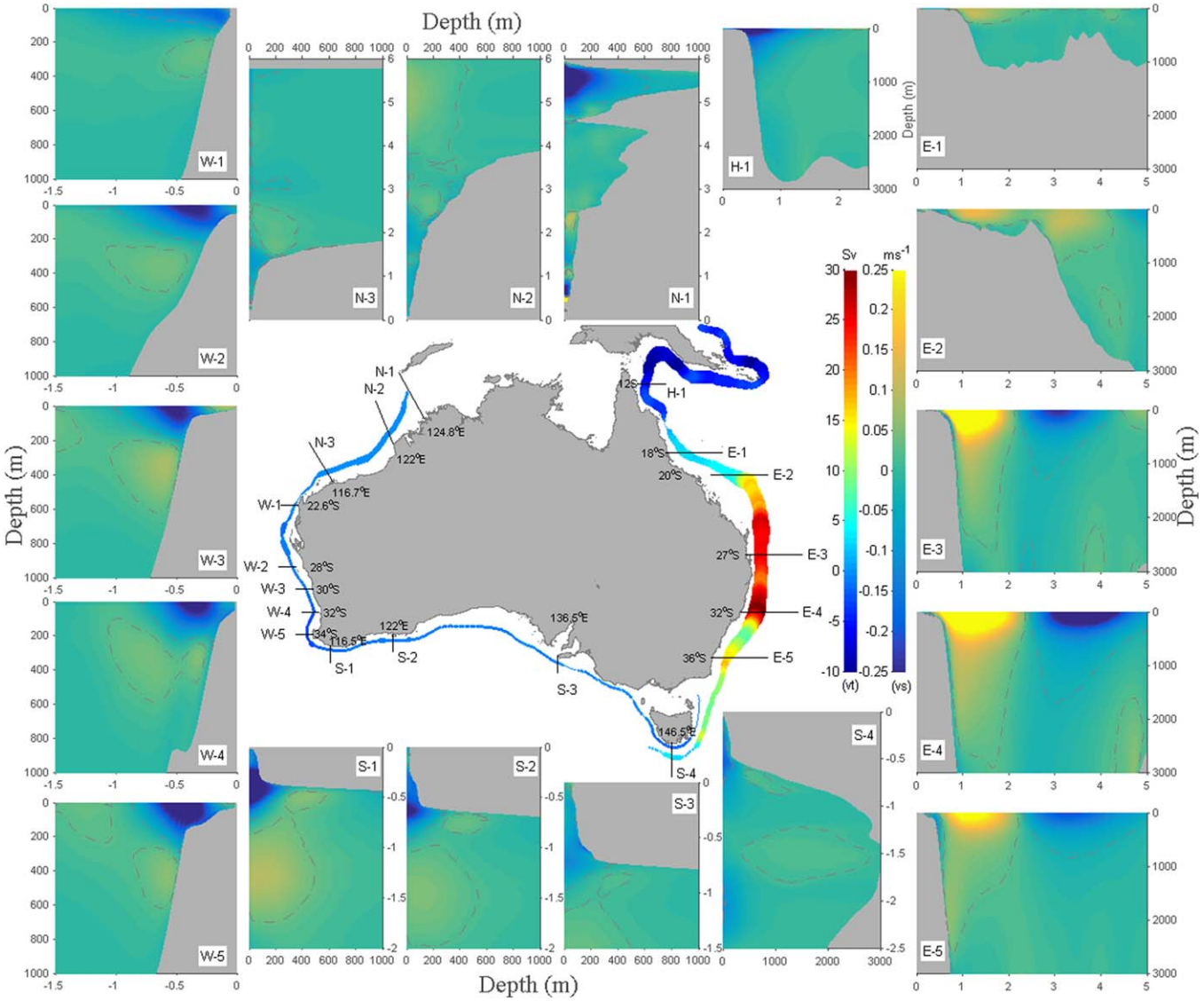


**Figure 3.** Vertical structure and mean (2000–2014) velocity and transport along the shelf/slope regions around Australia. Clockwise (anticlockwise) flow directions are shown as positive (negative). Color bars "vt" represent transport along the shelf/slope and "vs" is for velocity in the vertical. Contour line denotes $-0.02$ ms$^{-1}$ and 0.02 ms$^{-1}$.

Simulations reported here were undertaken over a 15 year period from 1 January 2000 to 31 December 2014. The model was initialized using HYCOM data, and the model was run for 6 months (June–December 1999) as spin-up. To prevent significant drift of sea surface temperature and salinity, the simulated surface data (SST and SSS) were relaxed to daily surface fields derived from HYCOM. It should be noted that sea surface height was not relaxed in this model run, and thus the estimated mean sea levels could be used to compare with observed mean sea levels.

To examine the vertical structure of the surface and subsurface boundary currents, transects across the continental shelf/slope (including the deep ocean) were selected, mainly in regions where comparative information was available (Figure 3). Mean volume fluxes at 4 km transects perpendicular to the 250 m contour line on the shelf slope were estimated using this method.

### 2.2. Model Validation and Predictive Capability

The ozROMS simulations were validated using observational data and transport estimates listed in the literature. Estimates of monthly mean sea level variability using ozROMS were compared to observations from

tide gauges and satellite altimeters. Volume transport estimates of the major Australian boundary currents (HLC, LC, SAC, ZC, EAC, TO, and HC) and major oceanic inflows/outflows (ITF, SICC, SEC, TF) from ozROMS simulations were compared to estimates from data collected by the Integrated Marine Observing System (IMOS) cross-shelf current meter mooring arrays (supporting information Table S1) available from (https://portal.aodn.org.au/) and transport estimates from the literature. Simulated salinity and temperature profiles were compared with monthly gridded Argo data obtained from Roemmich-Argo (http://sio-argo.ucsd.edu/RG_Climatology.html) (Roemmich & Gilson, 2009).

#### 2.2.1. Monthly Mean Sea Level: Tide Gauges

Comparison between measured and estimated monthly mean sea levels, at 14 tide gauge sites around the Australian coastline and two offshore island sites (Figure 2) is shown in supporting information Figure S1. The Root Mean Square Error (RMSE) between the monthly mean estimated and tide gauge sea levels were $<$0.08 m along the Australian coastline sites and $<$0.1 m for the two offshore island sites with a mean across all sites of 0.07 m (supporting information Table S1). Standard deviation ratios were clustered near 1.0, indicative of comparable variance between model and observations (supporting information Table S2). The monthly mean water levels around Australia generally represent the seasonal variability in the boundary currents (e.g., Ridgway & Godfrey, 2015). Both tide gauge data and model results indicated significant seasonal sea level variations at all the sites. The maximum mean annual range ($\sim$0.8 m) of the monthly mean sea level signal, observed in inner Gulf of Carpentaria (Karumba, station 1, Figure 2), was reproduced by the model (supporting information Table S2). The model also estimated the southward propagation of the seasonal sea level signal along the west coast of Australia, where variations in monthly mean sea level (MSL) is due to steric effects associated with the LC (Feng et al., 2003; Pattiaratchi, 2011; Ridgway & Godfrey, 2015). The annual mean sea level at Fremantle (station 6) with maxima in May–June was 0.23 m and 0.24 m in the observations and in the model, respectively. Along the south-west coast (Stations 7&8; Figure 2), the estimated annual sea level signal was at a maximum in July with a mean range 0.15 m similar to those in the observations (supporting information Table S2). At the northeast coastal sites, Townsville and Cairns (stations 13 and 14), the model captured both the phase of the seasonal cycle and the annual range ($\sim$0.2 m) correctly. Here, the annual sea level signal was a maximum in March and minimum in September. The model slightly over estimated mean annual range at Brisbane (station 12) and under estimated at Spring Bay (station 9). Overall, the model captured the seasonal sea level patterns at all sites and reproduced $>$80% of the observed mean annual range (supporting information Table S2).

#### 2.2.2. Annual Mean Sea Level Component: Satellite Altimeter

In addition to the single point time series measurements (i.e., tide gauges), the estimated annual mean sea level component compared well with that obtained from satellite altimeter data (supporting information Figure S2): (1) there was a good agreement between altimeter and simulated large-scale patterns, with the larger annual amplitude on the Northern shelf and smaller amplitude on the Southern shelf; (2) annual component was $>$0.5 m for the inner part of the Gulf of Carpentaria in the altimeter and model estimates; (3) annual component along the southern Australian shelf region was small compared to that further offshore; (4) sea level variability associated with the major oceanic currents (North Equatorial Counter Current, Equatorial Counter Current, South Equatorial Counter Current, South Equatorial Current, South Java currents etc.) were reproduced; (5) altimeter and model estimates also show the mesoscale eddy fields, with strong eddy fields associated with spatial sea level variability associated with the EAC; (6) the model did not reproduce eddies at the exact locations as observed from altimeter data as data assimilation was not included in ozROMS, but it did reproduce the scale and variability as discussed below; (7) spatial distribution of the RMSE computed between the monthly mean sea levels derived from ozROMS and satellite altimeter data across the model domain for the whole simulation period indicated small RMSE values ($<$0.04 m over $\sim$60% and $<$0.08 m for $\sim$80%) of the model domain. RMSE values were slightly higher ($\sim$0.1 m) in the EAC region where the mesoscale eddy activity was strong. The RMSE distribution was consistent with that reported by Oke and Schiller (2007), where the RMS residual was $>$0.1 m for EAC region for both their control and data assimilation simulations.

#### 2.2.3. Volume Transport: Moorings

Estimated ozROMS volume transports were compared with observed estimates from IMOS cross-shelf current meter mooring arrays: ITF, Kimberley, Pilbara, Two Rocks, South Australia, and at 27°S off eastern Australia (Mooring Arrays M1–M6; Figure 2 and supporting information Table S1). The monthly mean velocity components from ozROMS and current meter records were rotated to alongshore and offshore components

**Table 1**
*(a) Comparison of Volume Transport Predicted by Model and Estimated From IMOS Mooring Arrays (see Figure 2) and (b) Predicted Mean Transport at Different Cross-Shelf Sections (See Figure 3) Over the Entire Simulation Period (2000–2014)*

(a)

| Section | Period | Data used to compare | Mean net transport (Sv) | | Standard deviation (SV) | | RMSE (Sv) |
|---|---|---|---|---|---|---|---|
| | | | Observation | Simulation | Observation | Simulation | |
| M1 | Jul 2010 to Dec 2014 | 37 months | 1.21W | 1.55S | 1.34 | 0.82 | 0.28 |
| M2 | Sep 2012 to Aug 2014 | 18 months | 0.76W | 0.73W | 0.47 | 0.39 | 0.26 |
| M3 | Mar 2012 to Aug 2014 | 22 months | 1.14W | 1.08W | 0.99 | 1.0 | 0.31 |
| M4 | Jan 2011 to Dec 2014 | 41 months | 2.1S | 2.27S | 1.91 | 1.90 | 0.32 |
| M5 | Jan 2011 to Sep 2012 | 17months | 1.14E | 1.08E | 1.00 | 0.99 | 0.29 |
| M6 | Apr 2012 to Aug 2013 | 18 months and 0–2000 m depth | 15.8S | 16.4S | 7.13 | 6.8 | 2.78 |

(b)

| Northern shelf | | | Western shelf | | | Southern shelf | | | Eastern shelf | |
|---|---|---|---|---|---|---|---|---|---|---|
| | Surface core | Subsurface core | | Surface core | Subsurface core | | Surface core | Subsurface core | Upper 2,000 m, core along the shelf slope | |
| N-1 (124.8°E) | 8.24 ± 4.3 W | | W-1 (22.6°S) | 1.44 ± 1.6 S | 0.76 ± 0.49 N | S-1 (116.5°E) | 2.68 ± 2.1E | 0.90 ± 0.52W | H-1 (12°S) | 6.9± 4.9N |
| N-2 (122°E) | 0.77 ± 0.4 W | 0.36± 0.28E | W-2 (28°S) | 2.91 ± 1.9 S | 1.67 ± 1.29 N | | Total westward FC transport = 7.2 ± 4.3 Sv | | E-1 (18°S) | 5.66± 4.5S |
| N-3 (116.7°E) | 1.07 ± 0.8 W | 0.39 ± 0.32 E | W-3 (30°S) | 2.5 ± 2.1S | 1.91 ± 1.38 N | S-2 (122°E) | 2.31 ± 2.2E | 0.64 ± 0.54W | E-2 (20°S) | 11.8 ± 3.1S<br>18.18 ± 6.7S[a] |
| | | | W-4 (32°S) | 3.1 ± 1.8 S | 1.56 ± 1.42 N | | Total westward FC transport = 6.92 ± 3.8W | | E-3 (27°S) | 17.2 ± 9.8S<br>26.94 ± 10.8S[a] |
| | | | W-5 (34°S) | 3.67± 2.7 S | 1.19± 0.89 N | S-3 (136.5°E) | 1.31± 0.7E | 0.36± 0.34W | E-4 (32°S) | 17.6 ± 9.8S<br>30.55± 14.5S[a] |
| | | | | | | S-4 (146.5°E) | 1.89 ± 1.8E | 0.18 ± 0.52W | E-5 (36°S) | 8.6 ± 4.7S<br>14.8 ± 5.1S[a] |

[a]Denotes inclusion of the EAC recirculation and transport in Sv.

at each mooring section based on the orientation of the continental shelf break locally. The mean velocity profiles were then gridded onto a 5 m vertical by 4 km horizontal rectangular grid using triangular (linear) interpolation. The model bathymetry was used to construct the vertical grid transects. Volume transports were estimated by summing each cell transport contributions over the entire grid or specific parts of the grid (e.g., for the mooring data, transport was calculated in between the first near shore and last offshore moorings). It should be noted observations only cover a subset of the ozROMS simulation period (Table 1). The quantitative comparison of temporal variability (seasonal cycle) of ozROMS estimated net transport with the moored measurements indicated good agreement (Figure 4), however, there were some short-term variations in transport magnitudes, with a duration of ~3 months, that were not fully captured by ozROMS (Figure 4). The ozROMS reproduced the observed transport with small RMSE and standard deviation (Table 1).

Both observations and ozROMS indicated that at the shallow stations along the ITF Timor section, the flow reverses between north-easterly and south-westerly winds (see also Bahmanpour et al., 2016). The ozROMS mean net transport through the Kimberley and Pilbara transects were comparable to that of the observational estimates (Table 1). The mean southward transport at Two Rocks mooring section (M4) was 2.1 Sv in the observations and 2.27 Sv in the simulation (Table 1). The ozROMS net mean transport across the South Australian mooring section (M5) was 1.08 Sv to the east that compared favorably with the estimate from the moorings (1.14 Sv). There was also a distinct seasonal cycle in the observations at M5 that was also reproduced by ozROMS (Figure 4e). The ozROMS net mean transport through the EAC 27°S transect (M6) was southward at 16.4 ± 6.8 Sv for the depth range 0–2,000 m compared well with the mooring data estimates of 15.8 Sv (Table 1a) during April 2012–August 2013 (Sloyan et al., 2016). The volume transport over the 15 year simulation was southward at 17.2 ± 9.8 Sv (Table 1, E-3). The mooring array estimates included more austral winter periods (Sloyan et al., 2016) when the EAC is generally weaker (Ridgway, 2007; Ridgway & Godfrey, 1997).

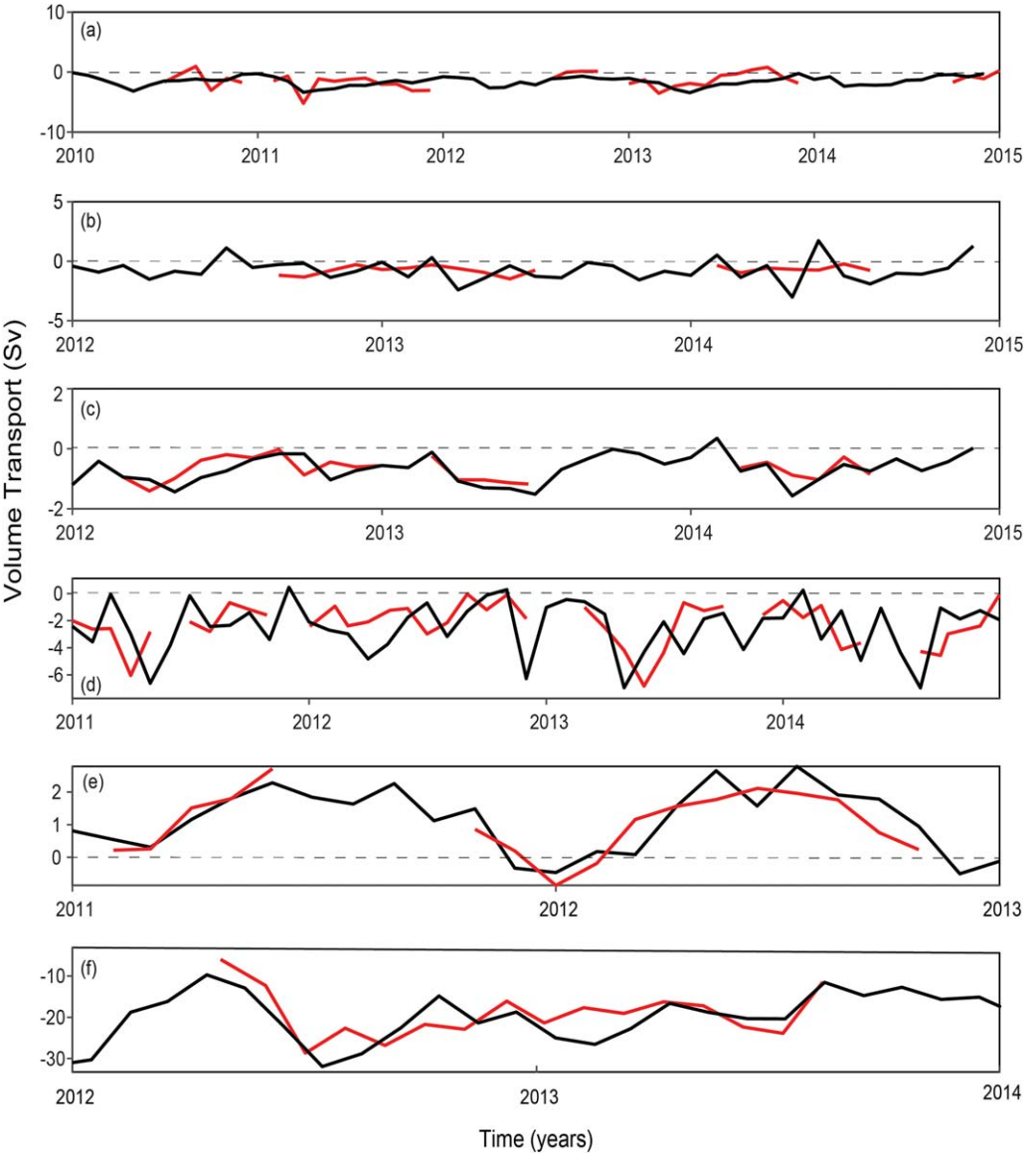


**Figure 4.** Time series of monthly mean transport estimated from ADCP mooring arrays (red) and ozROMS (black) at: (a) ITF shelf; (b) Kimberley; (c) Pilbara; (d) Two Rocks; (e) South Australia; and, (f) EAC at 27°S (see Figure 2 for location of the sections).

### 2.2.4. Volume Transport: Literature Sources

Comparison between volume transport estimated from ozROMS and those listed in the literature at specific locations within the model domain indicated good correspondence (supporting information Table S3). It should be noted that a direct comparison of ozROMS transport estimates with those in the literature was complicated by the diversity of measurement techniques, offshore extent, depth, time period, and the analysis method described.

Comparison with INSTANT mooring sections obtained between 2004 and 2006 (Sprintall et al., 2009) indicated that ozROMS reproduced the ITF transport estimates through the different passages within the Indonesian Archipelago (supporting information Table S3). The ozROMS mean transport through the Makassar Strait over the simulation period was 12.5 $\pm$ 6.2 Sv (supporting information Table S3). Estimated mean transport through the Makassar Strait during 2004–2006 was 13.2 $\pm$ 4.9 Sv (supporting information Table S3) in good agreement with estimates of 13.0 $\pm$ 3.8 Sv based on observations during INSTANT (Susanto et al., 2012). A large proportion of the ITF was transported through the Timor Passage (TP) with an annual mean

transport ~7.5 Sv (Metzger et al., 2010; Sprintall et al., 2009). The ozROMS mean transport through ITF Timor passage (ITF-TP) was confined to the northern part of the deep channel section close to the Indonesian coastline as per observations and the estimated mean transport was 8.2 ± 4.3 Sv (supporting information Table S3). The estimated (observed) mean outflow transport through Ombai and Lombok straits were 5.8 ± 2.7 Sv (4.9 Sv) and 1.8 ± 1.3 Sv (2.9 Sv), respectively (supporting information Table S3). The combined flow through the three passages provided an outflow of 15.8 Sv over the period 2000–2014 compared to observational estimates of ~10–15 Sv (supporting information Table S3) (Metzger et al., 2010; Sprintall et al., 2009; Susanto & Song, 2015). The ITF mean volume transport over the total water depth across a section along 115°E was 16.3 ± 8.6 Sv, in the range 9.7–17.5 Sv reported in the literature (supporting information Table S3). The estimated ITF transport in the upper 1,500 m over the period 2000–2014 was 14.7 Sv, similar in magnitude to that estimated by Feng et al. (2016) for the period 1979–2014 (13.5 Sv).

The ozROMS mean annual LC transport estimate at 32°S was 3.1 Sv, close to the estimate of Feng et al. (2016), 3.0 Sv. The ozROMS transport at 34°S (3.7 ± 2.7 Sv) was slightly lower than the 4.1 ± 2 Sv (1992–2006; supporting information Table S3) estimate by Schiller et al. (2008) at the same latitude. Only a few previous estimates of the SAC transport were available (1992–2006; supporting information Table S3) and ozROMS estimate at 130°E (~2.2 ± 1.4 Sv) was lower than the value (4.5 ± 2.6 Sv) reported by Schiller et al. (2008). At 122°E (Figure 3) the ozROMS estimate of 2.31 ± 2.2 Sv was higher than the 1.6 Sv reported by Feng et al. (2016). The ZC flow was confined to the continental shelf and the upper slope with an estimated transport through the southern Tasman transect (Figure 3) of 1.89 ± 1.8 Sv, slightly higher than the previous estimate of 1.1 ± 0.2 Sv (Baines et al., 1983). The mean transport of the FC at 115°E was 8.4 ± 3.6 Sv significantly lower than the 16 Sv reported by Middleton and Cirano (2002) but comparable to 9 Sv reported by Feng et al. (2016).

The EAC was associated with strong eddy and recirculation features and thus the volume transport estimates covered a wide range in the literature (supporting information Table S3). The ozROMS mean transport estimates at 27°S and 28°S were in agreement with previous estimates: at 32°S, including recirculation features the mean transport was 30.6 ± 4.5 Sv, smaller than the 36.8 ± 18.5 Sv quoted by Schiller et al. (2008). The estimated mean EAC transport between 18° to 35°S ranged between 12.6 Sv (excluding EAC recirculation) and 23.4 Sv (including EAC recirculation). Previous estimates of the mean transport between 18°S and 35°S ranged between 25 and 37 Sv (Mata et al., 2000; Ridgway & Dunn, 2003; Zilberman et al., 2014). The estimated TO, was 2.9 ± 2.4 Sv with estimates of TO encompassing a large range in the literature and van Sebille et al. (2012) reported values of ~4.2 ± 4.5 Sv.

#### 2.2.5. Salinity and Temperature: ARGO Monthly Profiles

The simulated salinity and temperature monthly mean climatology (2004–2014) data were gridded to Roemmich-Argo vertical and horizontal coordinates. Area mean monthly mean profiles of temperature and salinity profiles at nine selected regions were used to compare with Argo mean profile data. The ozROMS was found to be in good agreement with the Argo data in terms of mean temperature-salinity (T-S) properties in the oceans surrounding Australia (Figure 5). Argo and ozROMS profile data from January 2004 to December 2014 were used to calculate RMSEs and Bias at each depth (supporting information Figures S3 and S4). The simulated profiles indicated a good correspondence with the Argo profiles (RMSE for temperature and salinity $<2$°C and $<0.2$, respectively). However, it is important to note that intercomparison between different ARGO products around Australia (not shown) provided high RMSE's for salinity (0.3) and temperature (1.3°C). These values are similar to those found by Li et al. (2017) for the tropical Indian, Pacific, and Atlantic Oceans comparing Argo profiles those derived from moored observations.

## 3. Results

The results presented from a 15 year simulation (January 2000 to December 2014) of ozROMS with the model output averaged monthly to examine the boundary current structure, seasonal variability, and volume transport. The simulations also enabled the construction of a new schematic of the surface and subsurface boundary currents around Australia (Figure 6).

### 3.1. Boundary Currents

#### 3.1.1. Holloway Current (HLC)

The HLC flows to the south-west along the shelf edge of the north-west shelf and contributes to the LC (Figures 1a and 7a). The HLC extended to a depth of 100–200 m (Figures 3 and 7c) and was located close to the

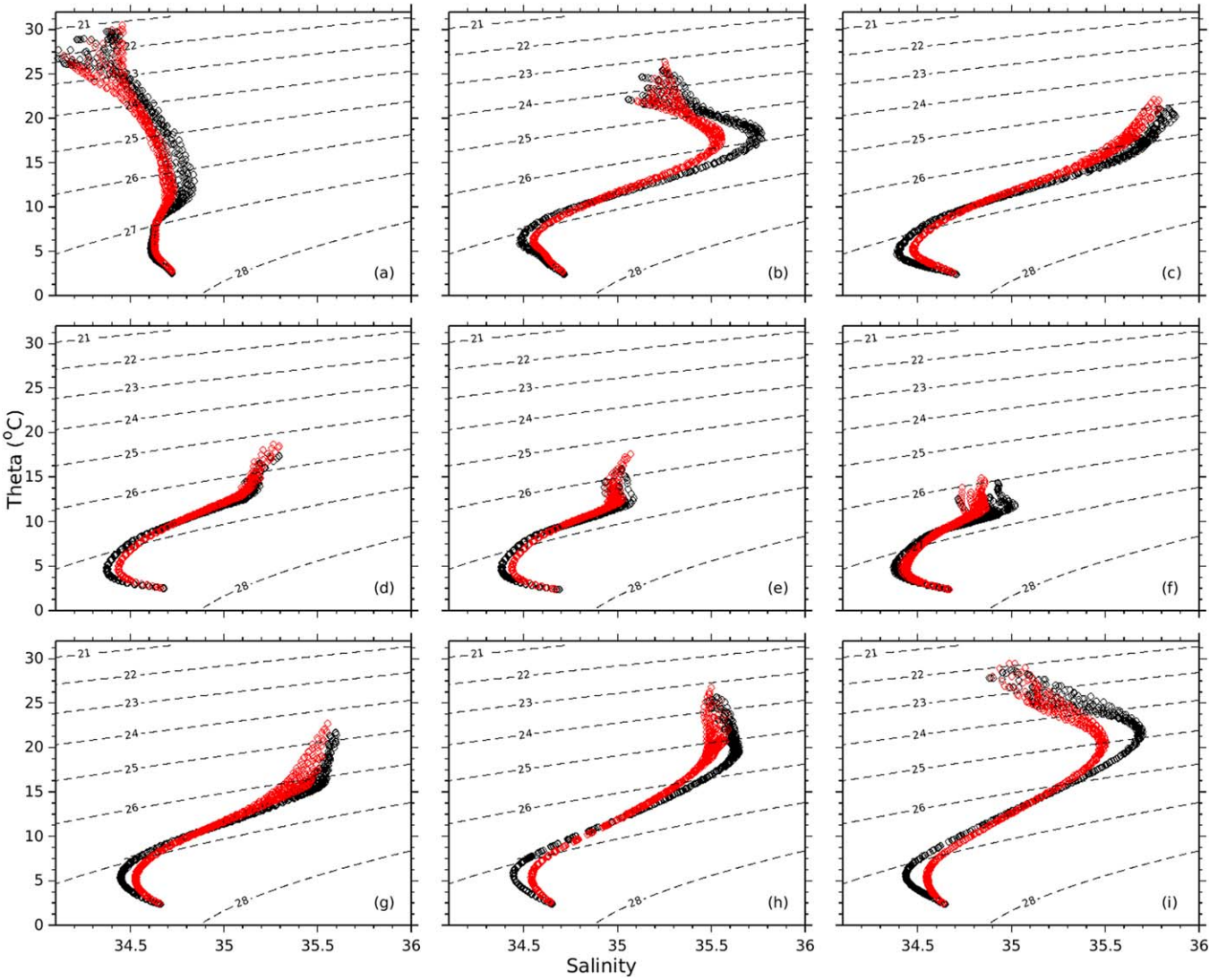


**Figure 5.** T-S diagrams of Argo data (black) and ozROMS (red) at nine regions around Australia. Panels (a) to (i) correspond to locations HG-(a) to HG(i) in Figure 2.

shelf-break. The HLC transport increased toward the south-west with the mean transport at the Kimberly and Pilbara transects (Figure 2) being $0.7 \pm 0.4$ Sv and $1.07 \pm 0.8$ Sv, respectively (Figure 6 and Table 1). There was a $\sim$0.3 Sv increase in mean transport between the Pilbara (N-2) and W-1 section ($1.44 \pm 1.6$ Sv southward). Model simulations allowed for the documentation of the seasonal and interannual variability of the HLC, previously identified as being a seasonal current that flowed mainly during the autumn (D'Adamo et al., 2009; Schiller, 2012). The HLC transport at the Kimberly transect (transect N-2) indicated significant seasonal variation, with a maximum of 1.8 Sv in April and a minimum of 0.4 Sv in January (Figure 8). The HLC transport along the Pilbara transect (transect N-3) was higher with a maximum of 3 Sv in May and a minimum of 0.4 Sv in February (Figure 8). The interannual variability of HLC at Pilbara was $\sim$0.8 Sv with transport maxima during the La Niña event in 2011–2013 and a minima during El Niño event in 2002 (Figure 9).

### 3.1.2. Leeuwin Current (LC) and Leeuwin Undercurrent (LU)

The beginning of the LC was defined by Ridgway and Condie (2004) to be the North West Cape (Figure 2). The depth integrated velocity in the upper 300 m indicated a continuity of flow from the north-west shelf southwards along the western coast, and flowing along the south coast (Figure 1a). The LC core depth increased southward from $\sim$150 m at North West Cape to $>$300 m at Cape Leeuwin (Figure 3). The southward LC transport through North West Cape section (transect W-1) was $1.44 \pm 1.6$ Sv slightly higher than

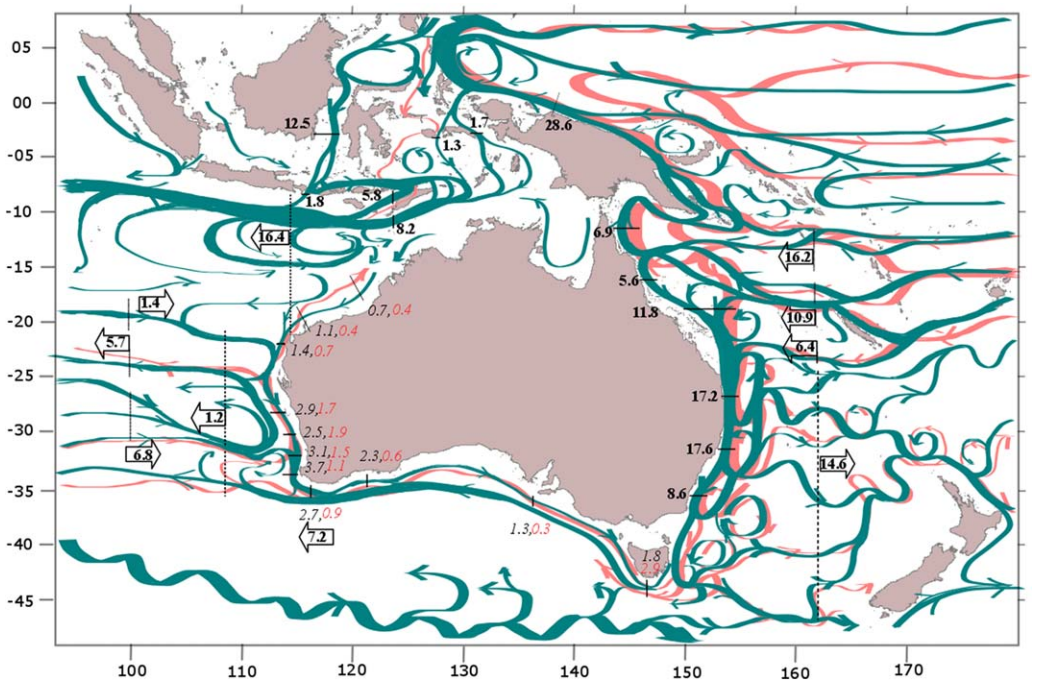


**Figure 6.** Schematic of major currents and mean transport (in Sv) estimates based on the long-term ozROMS simulation. Surface and subsurface currents/transports are represented by in green and red, respectively. Transports across major cross-sections are provided with surface and subsurface transport in black and red, respectively. Values inside arrows indicate meridional transport averaged over the dashed line associated with the arrow.

the transport of 1.07 ± 0.8 Sv through transect N-3 (Table 1). The transport across transect W-2 (at 28°S) was 2.91 ± 1.9 Sv, almost a threefold increase compared to that at W-1. The LC transport through transect W-3 was 2.5 ± 2.1 Sv and through W-4 was 3.1 ± 1.8 Sv. The seasonal range was 3.8 and 3.5 Sv at the W-3 and W-4 sections, respectively. Maximum estimated LC mean transport (∼4.12 Sv) occurred at 32.8° S between the W-4 and W-5. Transport through transect W-5 was 3.67 ± 2.7 Sv with high variability due to eddy activity and large (∼3.5 Sv) seasonal variability. The estimated mean transport between North West Cape (22.6°S) and Cape Leeuwin (34°S) was 2.6 Sv with an annual cycle with a mean range of 3.2 Sv. The LC transport along the western coast was a maximum in May–June and minimum in October (Figure 8). The transport increased from November to January with secondary minima in February (Figure 8). The strongest section of the LC was located at the southwest corner of Australia (Figure 1a and supporting information Figure S5) as it flowed past Cape Leeuwin (Figure 2) into the Southern Ocean. LC transport along the southern coast decreased slightly from west to east: from 2.68 ± 2.1 Sv at S-1(116.5°E) to 2.3 ± 2.2 Sv at S-2(122°E). Seasonal variability of the LC along the south coast was also large compared to the mean transport with a range of 2.8 Sv with a maximum in June–July, ∼1 month later than along the west coast (Figure 8). The interannual variability of LC transport was associated with the ENSO cycle (Figure 9, section W-5). The LC was weaker during El Niño years (2002–2003) and stronger in La Niña years (2011–2013). The monthly transport of the LC increased by ∼0.6 Sv and the annual mean transport by 0.8 Sv (∼25%) during the 2011–2013 La Niña event. Similar results were reported by Feng et al. (2016).

The LU, defined to be flowing northward along the west coast north of Cape Leeuwin (Figure 2) was present in the ozROMS simulations as a continuous subsurface boundary current in the depth range 300–800 m (Figure 3). The LU transport gradually increased from south to north (Figure 1b and supporting information Figure S6). The mean LU transport through W-5, W-4, and W-3 sections was 1.19 ± 0.89 Sv, 1.56 ± 1.42 Sv, and 1.91 ± 1.38 Sv, respectively. ozROMS estimated the maximum transport of the LU to be 2.4 Sv at 28.8°S slightly lower than the 3.4 Sv (supporting information Table S3) estimate by Furue et al. (2017) at the same latitude. In terms of seasonal variability, the LU was weaker in June at transect W-5; however, the seasonal signal was not clearly evident at other transects (Figure 8). At W-3, the estimated annual maximum (∼3 Sv) was in July. The LU split into two branches between 26°S and 24°S (supporting information Figure S6): (1)

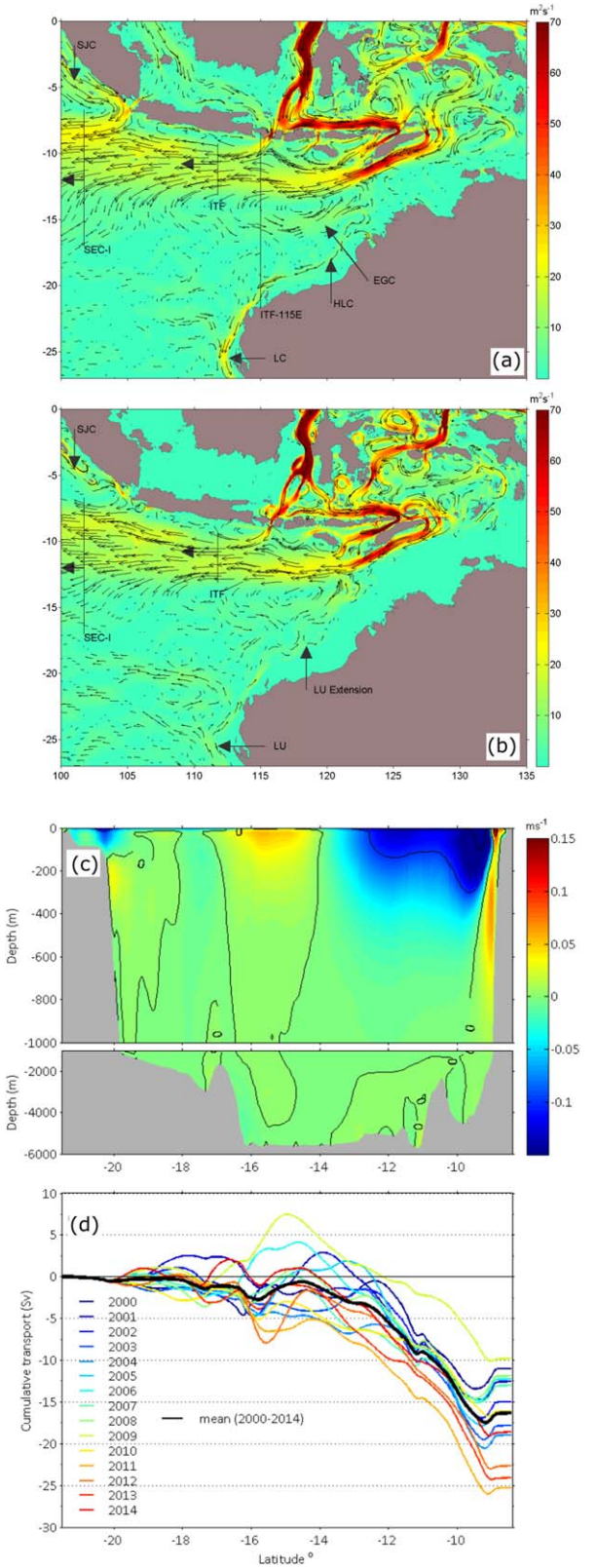


**Figure 7.** Estimates of transport between Northwest Australia and Indonesian coasts. Estimated mean vertically integrated currents between: (a) surface and 150 m depth; (b) 150 to 500 m depth; (c) mean zonal velocity section along 115°E; and, (d) annual mean cumulative volume transport variability over the full depth along 115°E section as a function of distance (latitude) from Australia.

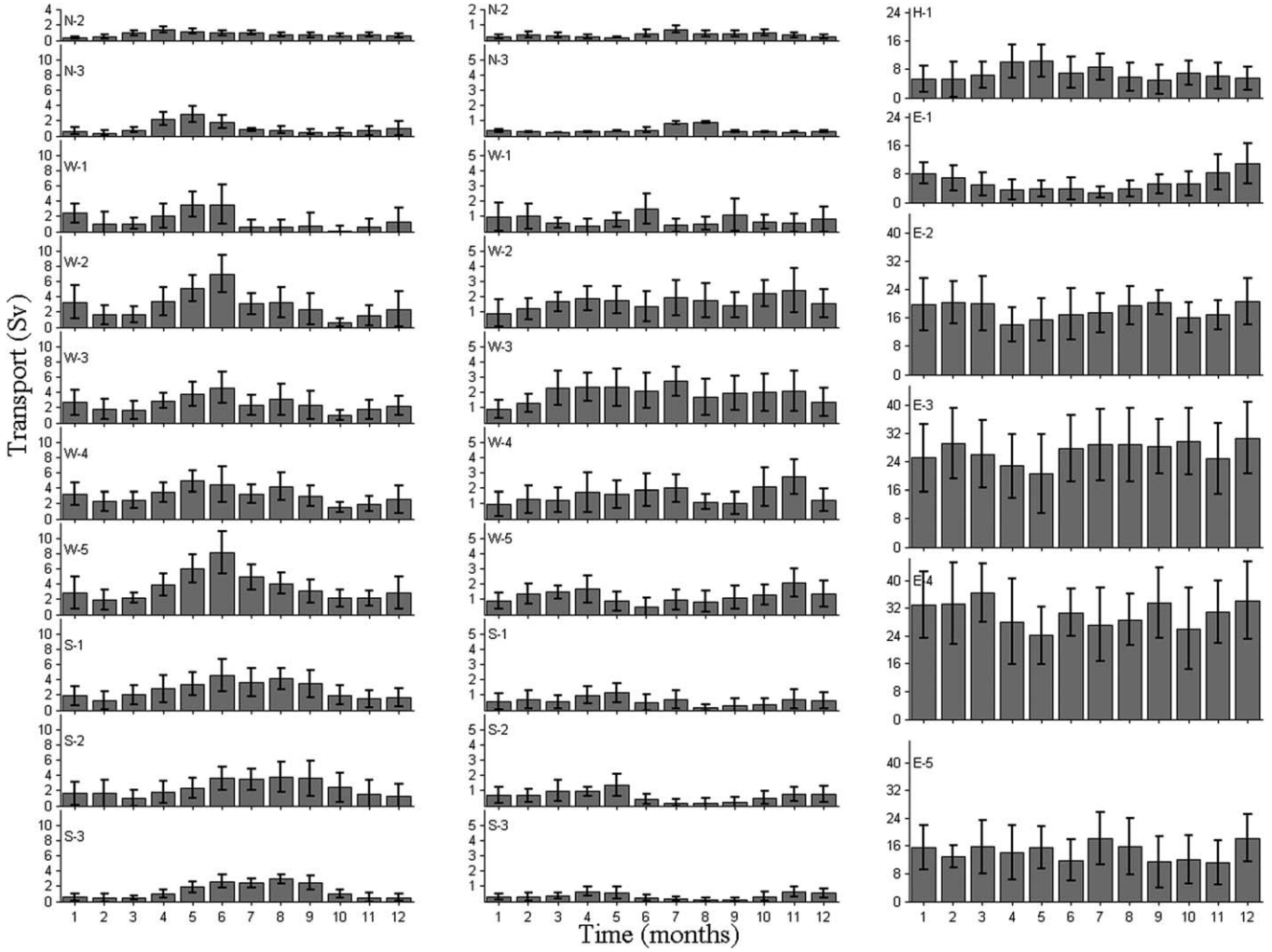


**Figure 8.** Seasonal variability (monthly means) of boundary current transport around Australia. (left: west and southern coasts): Holloway Current (N-2 and N-3), Leeuwin Current (W-1 to S-2), and South Australian Current (S-3); (middle: west and southern coasts) subsurface transport; and (right: east coast) Hiri Current (H-1), East Australian Current (E-1 to E-4), and EAC extension (E-5). The vertical black line represents the error bar.

flowing westward offshore; and, (2) continued along the continental slope toward the north and then northeastward with a transport of ~0.76 Sv at W-1 and ~0.4 Sv at N-2.

### 3.1.3. South Australian Current (SAC) and Zeehan Current (ZC)

The SAC is the continuation of the LC to the east (Figure 1a and supporting information Figure S7). The mean transport of the SAC at 136.5°E (S-3) was ~1.31 ± 0.7 Sv, with a mean seasonal range of ~2.5 Sv and a maximum in August–September, i.e., 4–5 months after the peak of HLC and 2–3 months after the peak in LC along the west coast (Figure 8). These peaks also reflected the progression of the seasonal mean sea level along the coast (Wijeratne et al., 2012). The SAC transport was also related to ENSO events with higher transport during 2011–2013 La Niña (Figure 9, section S-3).

The SAC eastward to the ZC was mainly confined to the continental shelf and the upper slope with transport through the southern Tasman transect (S-4) being 1.89 ± 1.8 Sv (Table 1), slightly higher than the previous estimate of 1.1 ± 0.2 Sv (Baines et al., 1983). The mean annual range of the transport was 2.8 Sv with maxima in September (Figure 8). The ZC flow continued eastward past southern Tasmania (Figure 1a).

### 3.1.4. Flinders Current (FC)

Along the southern coast, the simulations revealed the FC as the dominant flow extending from the surface to >1,000 m flowing westward from Tasmania and past Cape Leeuwin into the Indian Ocean (Figure 1 and supporting information Figure S7). Along the southern continental slope, the FC appeared as an

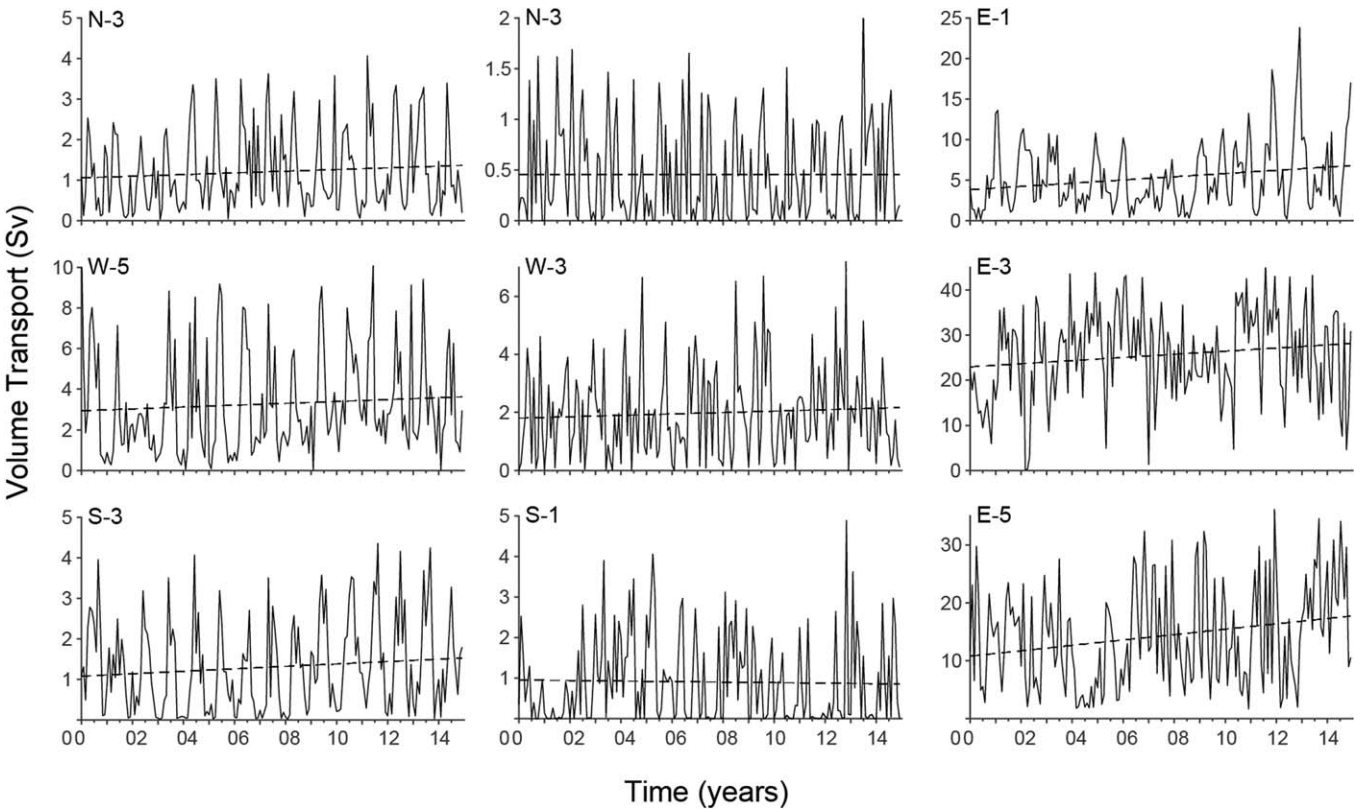


**Figure 9.** Estimated monthly mean surface and subsurface boundary current transport. Left plots: of Holloway Current (N-3); Leeuwin Current (W-5); South Australian Current (S-3); middle plots: under currents at N-3, W-3 and S-1; and right plots: East Australian Current (E-1 and E3); and, East Australian Current extension (E-5). Solid lines are monthly mean values and dashed lines represent the linear trend (see supporting information Table S4).

undercurrent beneath the eastward flowing LC, SAC, and ZC and a surface current further offshore (Figures 1 and 3) in agreement with field measurements (Akhir, 2009). The FC gradually intensified along its pathway from Tasmania to Cape Leeuwin (Figure 1b, supporting information Figure S7, and Table1) (see also Middleton & Cirano, 2002; Mueleners et al., 2007). The mean FC transport through S-2 (122°E) was 6.92 ± 3.8 Sv (Table 1) increasing to 7.2 ± 4.3 Sv at S-1 (116.5°E) and included a large seasonal (∼4.5 Sv) and strong (∼4 Sv) interannual variability. The subsurface (i.e., below the LC) westward FC volume transport at S-1 (0.9 ± 0.52 Sv) was slightly larger in magnitude at section S-2 (0.64 ± 0.54 Sv), but was a factor ∼3 larger than at section S-3 (0.36 ± 0.34 Sv) (Table 1).

#### 3.1.5. East Australian Current (EAC), Hiri Current (HC), and Tasman Front (TF)

The westward flowing SEC in the South Pacific Ocean was the main inflow into the EAC (Figure 1). Northern branches of SEC (North Vanuatu Jet (NVJ) and North Caledonia Jet (NCJ) interacted with the coast at ∼15°S and bifurcated: southward to form the EAC and northward to form the HC (Figure 1a and supporting information Figure S8). The HC formed a clockwise gyre in the Gulf of Papua and, along the Australian coast HC was a northward flowing current extending to depths >300 m (Figures 1 and supporting information Figure S8). At transect H-1 (12°S), the estimated mean northward transport of HC was 6.9 ± 4.9 Sv (Table 1) with a seasonal range of ∼5 Sv and was stronger in winter and weaker during summer (Figure 8). The mean southward transport of the EAC was 5.66 ± 4.5 Sv at E-1 (18°S) transect with a maxima in summer and a minima in winter (Figure 8). These results indicated that the northern branches of SEC inflow (NVJ and NCJ) contributed more to southward (northward) transport during summer (winter). The interannual variability of EAC at 18°S ranged between 2.5 and 9 Sv with higher transport during La Niña event of 2011–2013 (Figure 9). The seasonal range was also larger during 2011–2013 compared to the mean value. The seasonal signal was not clearly evident in the transport sections to the south (E-2 to E-5, Figure 8). An additional inflow to the EAC was derived from the EAC recirculation (northward flow to the east of the EAC) that contributed to the overall southward transport, particularly during winter, when the winds over Eastern Australia are stronger than in summer.

The EAC strengthened southward (Figure 3 and Table 1) and flowed continuously along the continental shelf and slope to ~32.5°S where flow separation occurred with ~60% of the eastward transport into the Tasman Basin as the TF. However, ~40% of the mean EAC transport in the upper layer continued along the continental slope to 35°S (Figures 1a, 6, and supporting information Figure S8), where it diverged from the coast as the southern TF. Major features of the EAC mean flow are the southward transport and the EAC recirculation (Figure 1 and supporting information Figure S8). The estimated southward (core) transport at transects E-2(20°S), E-3(27°S), and E-4(32°S) were 18.18 ± 6.7, 26.94 ± 10.8, and 30.55 ± 14.5 Sv, respectively. The net transport (excluding recirculation) associated with the E-4 section was 17.6 ± 9.8 Sv and similar to that at E-3 (17.2 ± 9.8 Sv). The net mean total southward transport over the full depth at E-3 section from coast to 157°E was ~ 4 Sv. The estimated maximum EAC transport was ~33.4 Sv (between 31° and 32°S), where the EAC recirculation was also dominant (Figure 1 and supporting information Figure S8).

#### 3.1.6. East Australian Current Extension and the Tasman Outflow (TO)

Subsequent to the EAC, flow separation from the coast at ~32°S the EAC extended southward (the "EAC extension") and was associated with cyclonic and anticyclonic southward moving eddy pairs (Figure 1 and supporting information Figure S8). In agreement with previous findings (Ridgway & Godfrey, 1997), the estimated mean currents generated by the eddy fields continued southward past Bass Strait and some flowed around Tasmania into the Eastern Indian Ocean as the TO (Figure 1). The net southward transport of the EAC at 33.5°S was ~12.4 Sv and, at 34°S ~9.8 Sv. At the E-5 (36°S) transect, eddy recirculation contributed to a large (14.8 ± 5.1 Sv) EAC core transport, while the estimated net southward transport was 8.6 ± 4.7 Sv (Table 1).

Along south Tasmania section (146.5°E, S-4), a small subsurface core of westward flow (~0.18 Sv) was evident. The core of westward flow (~2.8 Sv) was located further offshore with the total TO transport being ~2.9 ± 2.4 Sv (Table 1b). Previous estimates of TO varied significantly in the literature ranging between 3 and 10 Sv (supporting information Table S3). The important feature to note is the continuity of TO along the southern continental shelf and slope as an input into the FC which subsequently contributed to the LU with a continuation to the north-west of Australia (Figure 1b supporting information Figures S6 and S7).

### 3.2. Indian and Pacific Ocean Basin Inflows

#### 3.2.1. Indonesian Throughflow and EGC

The ITF was sourced from inflow from the North Pacific through the Makassar Strait and from the South Pacific through the Halmahera Sea (Figures 1 and 2). There was a small (~1 Sv) contribution from the South China Sea through the Karimata Strait. The ozROMS mean transport through Makassar Strait was 12.5 ± 6.2 Sv (Figure 6). Estimated mean inflow from the south Pacific through the Ceram Sea was ~1.3 Sv and the Lifamatola Strait was ~1.7 Sv (Figure 6) combining to contribute ~20% to the total ITF transport. The ITF reached a maximum during the southeast monsoon (June–August) and its interannual variability was associated with ENSO events (supporting information Figure S9) (see also: Gordon & Fine, 1996, Gordon et al., 2003, Potemra, 2005). ENSO events also influenced the distribution of flow through the different passages. The ozROMS simulations revealed that during the strong La Niña event of 2011–2013, inflows from both the North and South Pacific Ocean were higher than the mean with transports through Makassar Strait and Halmahera Sea being ~20.6 Sv (mean: ~12.5 Sv) and 3.8 Sv (mean: ~3 Sv), respectively (supporting information Figure S9).

The 115°E cross-section between Indonesia and Australia across the ITF indicated that the flow structure was limited to the upper 1,000 m with the following features (Figure 7c): (a) an eastward flowing South Java Current flowing close to the Indonesian coast extending to a depth of ~800 m; (b) the ITF in the upper 500 m extending from 3°S to 14°S; (c) the EGC between 14°S and 16.5°S the strongest flow in the upper 200 m; and, (d) along the Australian coastline, the westward flowing HLC present at the shelf edge and the LU extension along the continental shelf slope between 200 and 500 m (Figure 3) with a transport of ~0.4 Sv (Table 1). Similar signals were present in field observations (Bahmanpour et al., 2016). The estimated annual mean ITF transport (Figure 7d) varied between 10 and 24 Sv with a minima in 2009 (El Niño event) and a maxima in 2011 (La Niña event).

#### 3.2.2. South Indian Counter Current (SICC)

The South Indian Counter Current (SICC) originates in the western Indian Ocean to the south of Madagascar and propagates eastward as three branches (southern: sSICC, central: cSICC, and northern: nSICC) (Menezes et al., 2014; Palastanga et al., 2007). The nSICC was relatively weak in the ozROMS, crossing 100°E at ~15°S,

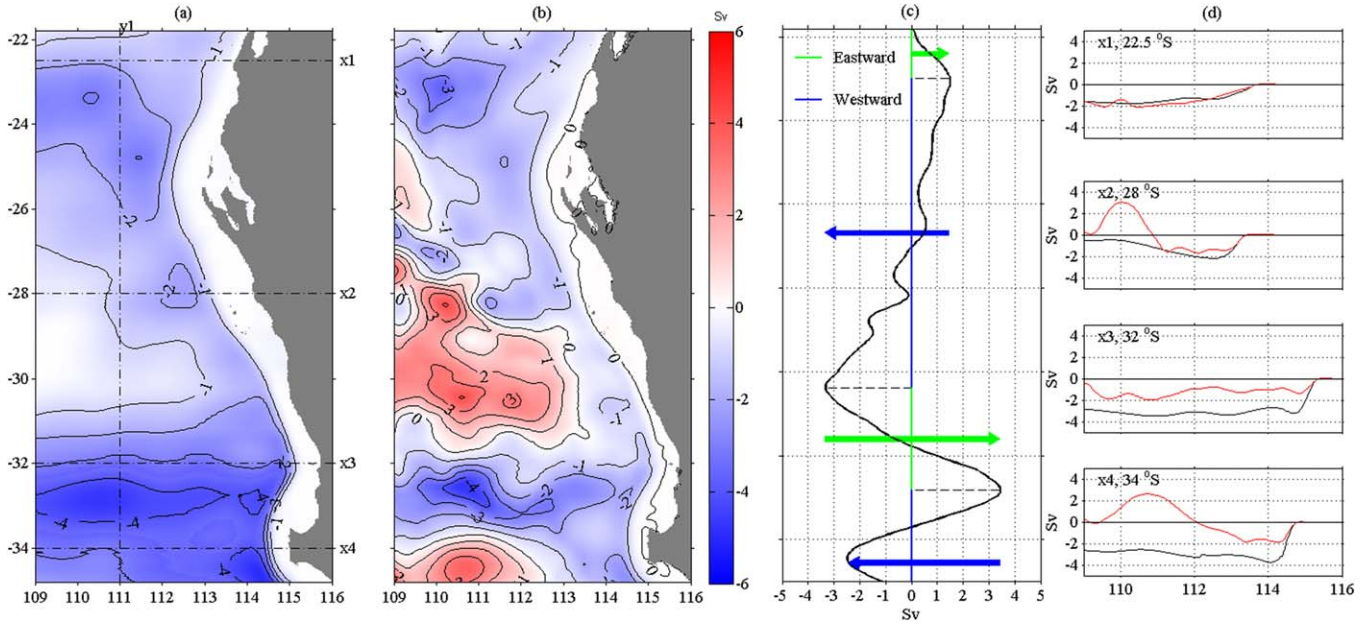


**Figure 10.** Estimated meridional cumulative volume transport as a function of distance from the west Australian coast. (a) 0–300m; (b) entire depth. Positive (negative) values denote northward (southward). (c) Cumulative zonal volume transport from north to south (negative values for westward and positive values for eastward) along the 111°E(y1) section in Figure 10a, arrows (blue and green) denote the main flow direction. (d) Cumulative volume transport as a function of distance from the coast at four sections (x1, x2, x3, and x4), where black lines represent 0–300 m and red lines full depth.

contributing to the Eastern Gyre (EG) (Figures 1 and 6). Meridional cumulative mean volume transport estimates identified the maximum inflow from cSICC and sSICC at 23°S and 31°S respectively in both depth ranges: 0–300 m and the entire depth (Figure 10). Estimated mean zonal transport of cSICC through 100°E was ∼1.4 Sv and extended to only ∼200 m depth.

### 3.2.3. Cumulative Transport: Eastern Indian Ocean

The cumulative southward transport indicated the mesoscale circulation features off Western Australia (Figure10). At 22°S there was an increase in the southward cumulative transport to 112°E which then remained almost constant to 109°E (x1; Figure 10d). At 28°S, within the surface 300 m, there was southward cumulative transport associated with LC from the coast to 111°E and a strong net northward transport between 111°E and 109°E (x2;Figure 10d). This northward transport formed part of the recirculation between sSICC and cSICC (Figure 6). There was cumulative transport southward at 32°S (x3; Figure 10d). Over the full depth, the transport was northward between 114°E and 111°E at 34°S. These transport pathways highlight two recirculation features: (1) the FC input into the sSICC indicated by the northward transport between 112°E and 119°E; and, (2) sSICC transport flowing northward and then offshore across 111°E. The mean eastward sSICC transport through 100°E was 6.8 Sv and ∼80% (5.7 Sv) of this transport was transported to the north and then west to form the broad eastern arm of the southern Indian Ocean basin gyre: the West Australian Current (see discussion).

### 3.2.4. South Equatorial Current (SEC)

Estimates of SEC transport, in the Pacific Ocean, vary widely in the literature and range between 27 and 54 Sv relative to 2,000 db (Rintoul & Sokolov, 2001). The total inflow from the SEC (NVJ + NCJ + SCJ), between 10°S and 26.5°S, across the 159.5°E meridional section was ∼33.5 Sv (Figure 11). At this section, the estimated NVJ(15–10°S), NCJ(22–15°S), and SCJ(26.5–22°S) transports were ∼16.2, 10.9, and 6.4 Sv respectively. At 159.5°E, the mean SEC annual transport ranged between 21 Sv in March and 40 Sv in September (supporting information Figure S10). There was also interannual variability (supporting information Figure S10): during the period 2000–2009 the annual range was ∼15 Sv. In contrast, during 2011–2013, the annual range was larger (∼24 Sv). Estimated net eastward transport through 159.5°E section between 26.5°S and 46°S (TF) was 14.6 ± 4.8 Sv (Figure 11c). Cumulative transport as a function of distance from the Australian coast revealed that the NVJ and NCJ inflow to EAC were from two pathways (Figure 11 and supporting information Figure S8): (1) between the coast and 148°E; and, (2) an offshore pathway between 152°E and 154°E.

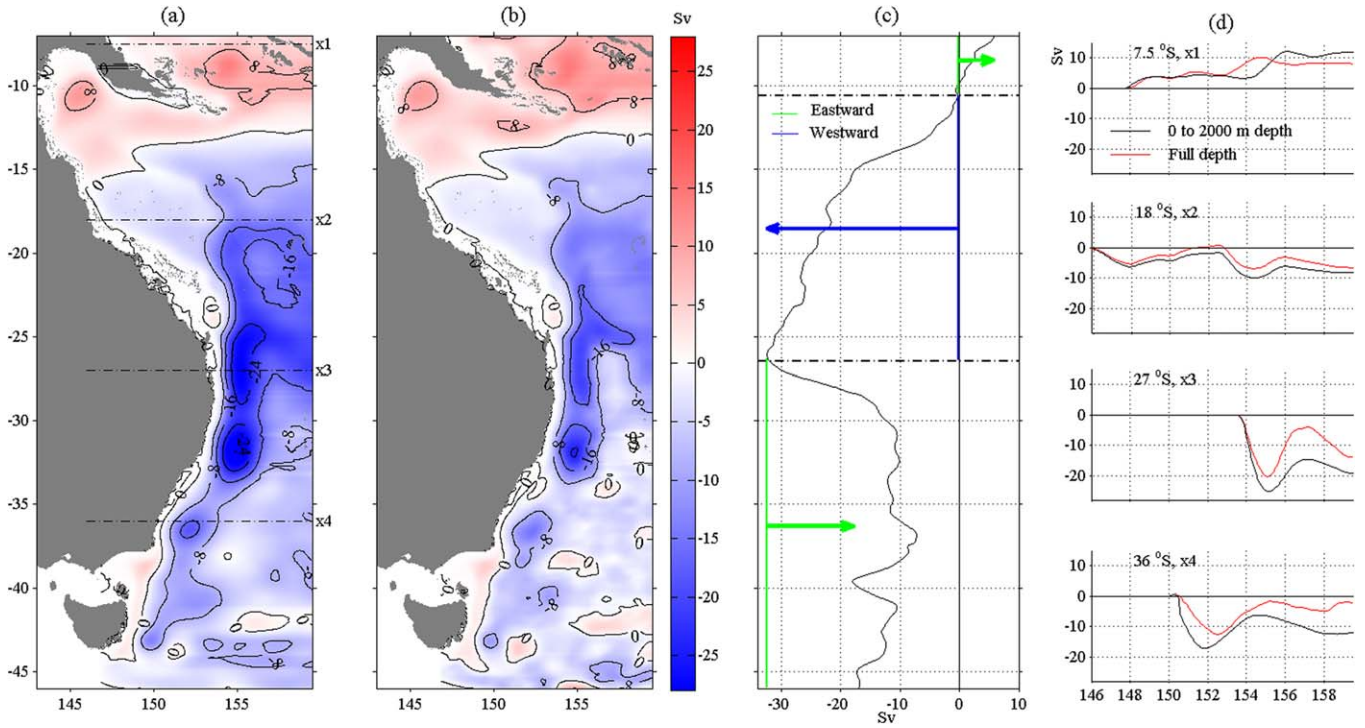


**Figure 11.** As Figure 10 but for the east coast. (a) 0–2,000 m and, (b) full depth. (c) Cumulative zonal volume transport from north to south along the 159.5°E section, arrows (blue and green) denote the main flow direction. (d) Cumulative volume transport at four sections (x1, x2, x3, and x4), where black lines represent 0–2,000 m and red lines full depth.

This was highlighted in the cumulative transport across 18°S (x2; Figure 11d) where there were two maxima in the southward transport: at 148°E and 154°E. This structure was also evident in the vertical velocity distribution at 20°S (Figure 3, E-2). Bifurcation of flow from the northern branches of the SEC (NVJ + NCJ) occurred between 12°S and 16°S (Figures 11a and 11b).

#### 3.2.5. Cumulative Transport: Western Pacific Ocean

Cumulative transport across the EAC and EAC extension indicated a reversing flow pattern with both southward and northward circulation with the latter associated with the EAC recirculation (Zilberman et al., 2014). At 18°S EAC transport extended from the coast to 148°E with the EAC recirculation (northward) between 148°E and 152°E (x2; Figure 11d). At 27°S, the EAC transport was from the coast to ~155°E and the EAC recirculation between ~155°E and 157°E (x3; Figure 11d). The ozROMS estimate of ~9 Sv for the mean EAC recirculation transport at 27°S (Table 1) was higher than the 6.3 Sv reported by Sloyan et al. (2016). Analysis of the mooring array at 27°S revealed that occasionally the EAC recirculation extended offshore of the mooring array (155.30°E) and was stronger/similar magnitude to that of the poleward EAC transport (Sloyan et al., 2016). The ozROMS transport estimate of 13 ± 4.9 Sv (Table 1) for the EAC recirculation at 32°S was similar (16 ± 3.6 Sv) to that by Zilberman et al. (2014). The EAC recirculation was also present offshore of the EAC extension at 36°S (0–2,000 m) with EAC transport extended from the coast to 152.5°E and the EAC recirculation between ~152.5°E and 154.5°E (x4; Figure 11d).

## 4. Discussion and Summary

As would be expected for an island continent, there was strong connectivity in the surface and subsurface current systems around the continent (Figure 6). At the surface, in the west of the continent, ITF inflow to the HLC and then to LC extended along the west and south coast to Tasmania via the SAC and ZC. In the South Pacific Ocean, the SEC was the main inflow into the EAC. Northern branches of SEC (NVJ and NCJ) interacted with the coast at ~15°S and bifurcated: southward to form the EAC and northward to form the HC. The EAC extension transported water past Tasmania and contributed to the FC (Figure 6). The FC is a surface current offshore of the LC and an undercurrent beneath the LC and contributed to the LU along the

west coast. The LU extended to the north-west shelf region and interacted with the EGC. Major inflows to the boundary currents were from the ITF, SEC and the SICC.

The volume transport rates and pathways around the Australian continent are summarized in Figure 6 while the estimates given in the literature are in supporting information Table S3. The net ITF inflow to the Indian Ocean was ~16.4 Sv with ~50% transported through Timor Passage. The combined eastward transport of the cSICC and sSICC was ~8.2 Sv across 100°E with the majority (>80%) of transport through sSICC.

The HLC is initiated from EGC at ~15°S and its transport increased toward the south-west (~1.4 Sv) at southern end, contributing to the LC at North West Cape (Figure 6). The LC transport increased >60% along the west coast between North West Cape (1.4 Sv) and Cape Leeuwin (3.7 Sv). The SAC mean volume transport was 50% of that of the LC but with a larger seasonal cycle (~2.5 Sv). The ZC mean transport was slightly larger than SAC. There were clear seasonal signals in the HLC, LC, SAC, and ZC transport that propagated along the coast. The HLC at North-west Cape was at a maximum in April–May while the LC maximum was in May–June, SAC peaked in August and ZC peaked in September. The minimum LC transport along the west coast was in October and increased from November to January with a secondary minimum in February (Figure 8).

The ozROMS output estimated the mean transport of the combined SEC (NVJ + NCJ + SCJ) westward at the 159.5°E section as ~33.5 Sv (Figure 6), of which ~12.2 Sv was transported northward (the HC transported ~7 Sv and ~5.2 Sv was transported directly from the Coral Sea to the Solomon Sea) and ~18 Sv southward into the EAC. The EAC transport increased from 5.6 to 17.6 Sv (a factor ~3) between 18°S and 32°S and separated offshore at ~32.5° with 40% of the transport continuing along the coast to 35°S (Figure 6). Through the EAC extension, ~ 25% of mainly deep (below 400 m) EAC water leaked to the Indian Ocean via the TO. The surface EAC extension (75% of total transport) turns eastward and contributed to the southern TF. The mean TO transport was ~2.9 Sv (~17% of total EAC) with a large standard deviation (2.4 Sv). The TO contributed to the FC along the southern shelf with the FC transport increasing by a factor 3 between Kangaroo Island and Cape Leeuwin through inflow from the south (Figure 6). The FC splits into two arms at Cape Leeuwin with one pathway flowing north beneath LC as the LU and other joining the sSICC. As LU flows northward ~75% of the transport flowed offshore between 24 and 29°S while ~25% continued to the northwest (Figure 6).

The response of the LC to ENSO events has been well documented: LC is stronger during La Niña and weaker during El Niño (Feng et al., 2003; Pattiaratchi & Buchan, 1991). Similarly, Middleton et al. (2007) reported transport of the SAC increased by a factor 2 between El Niño and La Niña events. In contrast, the ENSO influence on the EAC is not well established (e.g., Holbrook et al., 2011). The ozROMS simulations revealed that all Australian surface boundary current systems were enhanced during the 2011–2013 La Niña (Figure 9). The coastal sea levels have been used as a proxy for determining the strength of the boundary currents, particularly for the LC (Feng et al., 2003; Pattiaratchi & Buchan, 1991). The monthly mean water levels (both observations and predictions) indicated higher water levels during 2011–2013 (supporting information Figure S1). It should be noted that the 2011–2013 La Niña is one of the strongest events experienced in recent decades.

Feng et al. (2016) indicated that the volume transports of major ocean boundary currents around Australia consisted of an increasing trend over the period 1979–2014. ozROMS also predicted this increasing trend for all boundary currents with the mean annual trends for the LC, SAC and EAC that were slightly higher than reported by Feng et al. (2016) (supporting information Table S4). The mean annual trend difference between Feng et al. (2016) and ozROMS may be impacted by the time window of the studies (ozROMS: 2000–2014; Feng et al., 2016: 1979–2014).

### 4.1. Indonesian Throughflow (ITF) and Eastern Gyral Current (EGC) Inflows to HLC

Approximately 76% (~12.5 Sv) of the ITF was derived from inflow from the North Pacific through the Makassar Strait and ~18% (~3 Sv) from the South Pacific through Halmahera Sea (Figure 6). The surface intensified inflow through Halmahera Sea enters into the Indian Ocean via Timor Passage (Figures 6 and 7) (see also Frederic et al., 2013). Simulations revealed that the ITF has strong seasonal variations through both pathways. These findings were consistent with the results of other investigators (Gordon & McClean, 1999; Sprintall et al., 2009; Susanto & Song, 2015). ozROMS has confirmed the previous finding that increased ITF

transport through Makassar Strait under La Niña conditions and reduced transport during El Niño (Susanto et al., 2012). Interannual variability through Halmahera Sea has not been well documented in the literature. However, ozROMS simulations indicated that during La Niña events (2011), flow through Halmahera Sea was also enhanced (supporting information Figure S9). Sprintall and Revelard (2014) suggested that the Pacific ENSO variability is strongest in Timor Passage, most likely through the influence of planetary waves transmitted from the Pacific along the Northwest Australian shelf pathway.

Along the northwest shelf, the HLC was initiated (see also Bahmanpour et al., 2016) through flow from ITF (through Timor Passage) with additional inflow from EGC (Figure 7). There is confusion in the literature with regard to the role of the Eastern Gyral Current (EGC). Menezes et al. (2016) suggested the EGC as a partial retroflection of the SEC and continuation of the nSICC (Figure 6). Others (e.g., Domingues et al., 2007; Feng et al., 2003; Meyers et al., 1995) identified the Eastern Gyral Current (EGC) as an input to LC at North West Cape. In ozROMS the EGC was flowing east at 100°E between latitudes 15°S and 18°S and was mostly confined to the upper 200 m (Figures 7a–7c) consistent with Menezes et al. (2013, 2014, 2016). ozROMS also confirmed the Menezes et al. (2016) finding that the EGC is a continuation of the nSICC. A significant proportion of the EGC recirculated into the ITF/SEC to complete the anticyclonic EG circulation whilst a proportion of EGC contributed to the HLC and filaments of the EGC also contributed to the HLC along the Australian coast north of North West Cape (Figure 7a). The increased HLC transport between the Kimberly (N-2) to North West Cape (W-1) can be attributed to the inflow from the EGC.

Model simulations allowed for the documentation of the seasonal and interannual variability of the HLC, previously identified as being a seasonal current that flowed mainly during the autumn (Brink et al., 2007; Cresswell et al., 1993; D'Adamo et al., 2009; Holloway, 1995; Holloway & Nye, 1985). In agreement with observations (Bahmanpour et al., 2016), ozROMS predicted that HLC flows throughout the year, strongest in April/May and weaker in September. Menezes et al. (2013) found that the EGC transport variations have the same phase as the LC, and, consequently, the eastward currents driven by salinity gradients were essential components for understanding the poleward-flowing LC. In a recent study, Ridgway and Godfrey (2015) suggested that the monsoon wind setup sea levels on the Gulf of Carpentaria (GC) controlled the seasonality of the LC. In ozROMS, HLC accounted for ∼70% of the seasonal variance of LC, SAC and ZC in agreement with Yit Sen Bull and van Sebille (2016). A small secondary maximum in transport occurred in January (summer) for HLC, LC, and SAC. Minimum transport for the HLC occurred in August, LC in October and SAC in November a similar lag effect to that for the maximum transport. The LC is stronger in winter and weaker in summer (e.g., Feng et al., 2003; Pattiaratchi & Woo, 2009). ozROMS indicated that although the maximum LC transport occurred in winter (June, Figure 8) there was a smaller modulation of the transport with a minimum in October increasing from November to January and then decreasing in February. This pattern is reflected in the seasonal coastal sea levels, a measure of the LC strength (see supporting information Figure S1 and Pattiaratchi, 2011). The seasonal cycle of LC is attributed to the combination of two processes: (1) monsoon wind setup of sea level in the Gulf of Carpentaria (Ridgway & Godfrey, 2015); and, (2) seasonal influence of EGC (Menezes et al., 2013).

### 4.2. South Indian Counter Current (SICC) Inflows to LC and LU

The northern input to the LC (previously identified as EGC; De Deckker et al., 2012; Domingues et al., 2007; Feng et al., 2003; Waite et al., 2007) was from cSICC (Figures 1a and 6). The cSICC was located between 18°S and 23°S with mean transport ∼1.4 Sv across 100°E. Increase in LC transport between transects W-1 and W-2 (Table 1) can be attributed to the inflow from the cSICC that feeds the LC between 22°S and 24°S (see also Lambert et al., 2016). The southern SICC (sSICC) flows almost zonally from Madagascar to Australia along ∼26°S, with a slight poleward orientation (Lambert et al., 2016; Menezes et al., 2014). There was an increase of ∼1.2 Sv in the southward transport in the LC between transects W-3 and W-5 where the sSICC input to the LC (Table 1). The ozROMS estimated > 60% of LC was sourced from cSICC and sSICC as reported by Yit Sen Bull and van Sebille (2016).

The traditional view of subtropical gyre circulation of the south Indian Ocean prescribes the West Australian current (WAC) as the eastern boundary current. However, the presence of the LC modifies this circulation and the location of the WAC is not well defined in the recent literature. ozROMS simulations identified offshore transport (∼5.7 Sv) between the cSICC and sSICC that may be identified as part of the WAC. Here, ∼80% of the sSICC flow moves northwards and then offshore (Figure 6). This is in contrast to the conclusion

from Furue et al. (2017) who proposed that a large component of the SICC inflow (3.4 Sv) to the LC is "lost" through downwelling.

Water mass analyses indicated that the FC and LU have similar characteristics and were associated with the sub Antarctic Mode water (Akhir, 2009; Woo & Pattiaratchi, 2008). The model output confirmed this connection with the FC bifurcating to the west of Cape Leeuwin and feeding into the LU through two separate pathways: (1) flow around Cape Leeuwin with direct input to LU (Figure 1b and supporting information Figure S6); and, (2) FC flowing westward into the Indian Ocean (Figure 1 and supporting information Figure S6) and then looping northward and combining with sSICC and input to the LU at around 32°S and increasing the LU transport (supporting information Figure S6). These two flow patterns are consistent with those reported by Furue et al. (2017). The LU was ~1 Sv at Cape Leeuwin (Figure 6) and the maxima of ~2.4 Sv of LU (supporting information Table S3) estimated at 28.8°S was derived from ~1.4 Sv inflow from sSICC. Further north, the cSICC being a shallow current (<200 m) did not directly contribute to LU.

### 4.3. South Equatorial Current (SEC) Inflows to EAC and Eddy-Recirculation

In the Pacific Ocean, northern branches of SEC (NVJ and NCJ) interacted with the coast at ~15°S and initiated the HC and EAC (Figure 1; see also Godfrey et al., 1980). The HC and EAC have different seasonal cycles: the EAC is a maximum in December–January while HC peaks in June–July. This indicated that the northern branches of SEC inflow (NVJ and NCJ) contributed more to southward (northward) transport during summer (winter). Previous studies have suggested that the majority of the NVJ and NCJ water that flowed into the Coral Sea, turned northward and flowed to the Solomon Sea (Gasparin et al., 2012; Kessler & Cravatte, 2013). These studies suggested that the EAC was sourced mainly from the SCJ interacting with the Australian coastline between 23°S and 25°S (Figure 1 and supporting information Figure S8). However, ozROMS simulations indicated that a significant component (~11.8 Sv) of the EAC transport was from NVJ and NCJ inflow between 15°S and 22°S (Figure 6). Southward transport of the EAC increased from 11.5 Sv at 20°S to 17.2 Sv at 27°S. To achieve the estimated transport at E-3 of 17.2 Sv (Table 1), an inflow of ~5.7 Sv was required via SCJ. ozROMS simulations indicated that inflow from SCJ was mostly confined to the subsurface and transported ~6.4 Sv, in good agreement with the estimate of ~8 Sv by Kessler and Cravatte (2013). Thus SEC inflow to the EAC can be attributed as 65% via NVJ and NCJ and 35% via SCJ.

In summary, the shelf-scale 3-D hydrodynamic model ozROMS realistically simulated the boundary currents around Australia consistent with the available observations. Simulations also clarified some areas of uncertainty listed in the literature as well as new information on circulation pathways that was previously unknown that are summarized below (see also Figure 6):

1. The ITF is sourced from inflow from the North Pacific through the Makassar Strait and from the South Pacific through Halmahera Sea. During La Niña events, flow through Halmahera Sea was enhanced.
2. EGC is a continuation of the nSICC with inflow directly onto the HLC at ~15°S. The northern input to the LC was from cSICC.
3. HLC flows throughout the year, strongest in April/May and weaker in September. The HLC transport was weaker (stronger) during El Niño (La Niña) events.
4. There were clear seasonal signals in the HLC, LC, SAC, and ZC transport that propagated along the coast with maxima in April/May, June, August, and September, respectively. Minimum transport for the HLC occurred in August, LC in October, and SAC in November.
5. The largest inflow (> 60%) to LC transport on the west coast was derived from two branches of the SICC between 22–24°S (cSICC) and 26–32°S (sSICC).
6. The West Australian current (WAC) was located between cSICC and sSICC. Here, ~80% of the sSICC flow moves northward and then offshore to the south of cSICC.
7. In the Pacific Ocean, northern branches of SEC (NVJ and NCJ) interacted with the coast at ~15°S and initiated the HC and EAC. The SEC inflow to the EAC can be attributed as 65% via NVJ and NCJ and 35% via SCJ.
8. The TO contributed to FC along the southern coast with the FC flowing as a subsurface current underneath the LC and a surface current further offshore.
9. The FC bifurcated west of Cape Leeuwin with one arm flowing northwards as the LU to north-west of Australia. The second arm flowed north-west, combined with sSICC as an inflow to LU at ~32°S, enhancing its northward transport.

10. sSICC contributed ~60% of LU transport. As LU flows northward ~75% of the transport flowed offshore between 24°S and 29°S while ~0.4 Sv continued to the northwest flowing beneath the HLC and defined here as the LU extension that had a direct input to the EGC.
11. All boundary current transport was enhanced during the La Niña event in 2011–2013.

## 5. Conclusions

Long-term (15 year), high-resolution shelf-scale model (ozROMS) simulations were used to estimate the mean, seasonal, and interannual variability of the boundary currents, associated inflows and their connectivity. Using the same shelf-scale model for the whole Australian region allowed for estimates of transport using the same methodology. Transport estimates and the major circulation patterns were in broad agreement those obtained from moored instruments and with those listed in the literature. The ozROMS simulations confirmed the documented major circulation patterns, provided revised transport estimates and more importantly allowed for the definition and quantification of major inflows and their variability.

**Acknowledgments**
The study was funded by the Australian National Network in Marine Science (ANNIMS) springboard program with the title "Ocean-shelf exchange with an emphasis on the roles of waves, tides, eddies and cross-shelf flows." Access to the supercomputing facilities of the Pawsey Centre (Magnus) was enabled through the partner allocation scheme. The current meter data along the ITF, Kimberley, Pilbara, Two Rocks, South Australia, and the EAC were collected as part of the Integrated Marine Observing System (IMOS, www.imos.org.au), a national collaborative research infrastructure supported by the Australian Government. The current meter data are available through the Australian Ocean Data Network (https://portal.aodn.org.au). Daily mean three-dimensional currents, temperature, and salinity together with mean water levels available for the ozROMS simulations described in this paper is available through OPeNDAP: http://130.95.29.56:8080/thredds/catalog.html

## References

Akhir, M. F. M. (2009). *Physical processes along the southern continental shelf and slope of Western Australia* (PhD thesis). Crawley, WA: The University of Western Australia. Retrieved from: http://research-repository.uwa.edu.au/en/publications/physical-processes-along-the-southern-continental-shelf-and-slope-of-western-australia(94f352c5-5052-407d-9e90-d6432800c5db).html

Bahmanpour, M. H., Pattiaratchi, C., Wijeratne, S., Steinberg, C., & D'adamo, N. (2016). Multi-year observation of the Holloway current along the shelf edge of north-western Australia. *Journal of Coastal Research*, *75*, 517–521.

Baines, P. G., Edwards, R. J., & Fandry, C. B. (1983). Observations of a new baroclinic current along the western continental slope of Bass Strait. *Australian Journal of Marine and Freshwater Research*, *34*, 155–157.

Bowen, M. M., Wilkin, J. L., & Emery, W. J. (2005). Variability and forcing of the East Australian Current. *Journal of Geophysical Research*, *110*, C03019. https://doi.org/10.1029/2004JC002533

Brinkman, R., Wolanski, E., Deleersnijder, E., McAllister, F., & Skirving, W. (2001). Oceanic inflow from the Coral Sea into the Great Barrier Reef. *Estuarine Coastal and Shelf Science*, *54*, 655–668.

Castelao, R., Chant, R., Glenn, S., & Schofield, O. (2010). The effects of tides and oscillatory winds on the subtidal inner-shelf cross-shelf circulation. *Journal of Physical Oceanography*, *40*, 775–788. https://doi.org/10.1175/2009JPO4273.1

Cetina-Heredia, P., Roughan, M., van Sebille, E., & Coleman, M. (2014). Long-term trends in the East Australian Current separation latitude and eddy driven transport. *Journal of Geophysical Research: Oceans*, *119*, 4351–4366. https://doi.org/10.1002/2014JC010071

Chapman, D. C. (1985). Numerical treatment of cross-shelf open boundaries in a barotropic coastal ocean model. *Journal of Physical Oceanography*, *15* (8), 1060–1075.

Chassignet, E. P., Hulburt, H. E., Smedstad, O. M., Halliwell, G. R., Hogan, P. J., Wallcraft, A. J., et al. (2007). The HYCOM (HYbrid coordinate ocean model) data assimilative system. *Journal of Marine Systems*, *65*, 60–83.

Cresswell, G. (2000). Currents of the continental shelf and upper slope of Tasmania. *Papers and Proceedings of the Royal Society of Tasmania*, *133*, 21–30.

Cresswell, G., Frische, A., Peterson, J., & Quadfasel, D. (1993). Circulation in the Timor Sea. *Journal of Geophysical Research: Oceans*, *98*(C8), 14379.

D'Adamo, N., Fandry, C. S., Buchan, S., & Domingues, C. (2009). Northern sources of the Leeuwin Current and the "Holloway Current" on the North-west Shelf. *Journal Royal Society Western Australia*, *92*, 53–66.

De Deckker, P., Moros, M., Perner, K., & Jansen, E. (2012). Influence of the tropics and southern westerlies on glacial interhemispheric asymmetry. *Nature Geoscience*, *5*, 266–269.

Domingues, C. M., Maltrud, M. E., Wijffels, S. E., Church, J. A., & Tomczak, M. (2007). Simulated Lagrangian pathways between the Leeuwin Current system and the upper-ocean circulation of the southeast Indian Ocean. *Deep Sea Research Part II: Topical Studies in Oceanography*, *54* (8–10), 797–817.

Feng, M., Meyers, G., Pearce, A., & Wijffels, S. (2003). Annual and inter-annual variations of the Leeuwin Current at. *Journal of Geophysical Research*, *108*(C11), 3355. https://doi.org/10.1029/2002JC001763

Feng, M., Zhang, X., Oke, P., Monselesan, D., Chamberlain, M., Matear, R., et al. (2016). Invigorating ocean boundary current systems around Australia during 1979–2014: As simulated in a near-global eddy-resolving ocean model. *Journal of Geophysical Research: Oceans*, *121*, 3395–3408. https://doi.org/10.1002/2016JC011842

Flather, R. A. (1976). A tidal model of the north-west European continental shelf. *Memoires de la Societe Royale des Sciences de Liege*, *6*(10), 141–164.

Furue, R., Phillips, H. E., Mccreary, J. P., Jr., & Bindoff, N. L. (2017). On the Leeuwin current system and its linkage to zonal flows in the South Indian Ocean as inferred from a gridded hydrography. *Journal Physical Oceanography*, *47*, 583–601.

Gasparin, F., Ganachaud, A., Maes, C., Marin, F., & Eldin, G. (2012). Oceanic transports through the Solomon Sea: The bend of the New Guinea Coastal Undercurrent. *Geophysical Research Letters*, *39*, L15608. https://doi.org/10.1029/2012GL052575

Glorioso, P. D., & Simpson, J. H. (1994). Numerical modelling of the $M_2$ tide on the northern Patagonian Shelf. *Continental Shelf Research*, *14*, 267–278.

Godfrey, J. S., Cresswell, G. R., Golding, T. J., & Pearce, A. F. (1980). The separation of the East Australian Current. *Journal of Physical Oceanography*, *10*, 430–440.

Gordon, A. L., & Fine, R. A. (1996). Pathways of water between the Pacific and Indian Oceans in the Indonesian seas. *Nature*, *379*, 146–149.

Gordon, A. L., & McClean, J. L. (1999). Thermohaline stratification of the Indonesian Seas: Model and observations. *Journal of Physical Oceanography*, *29*, 198–216.

Gordon, A. L., Susanto, R. D., & Vranes, K. (2003). Cool Indonesian Throughflow as a consequence of restricted surface layer flow. *Nature*, *425*, 824– 828.

Haidvogel, D. B., Arango, H., Budgell, P. W., Cornuelle, B. D., Curchitser, E., Lorenzo, E. D., et al. (2008). Ocean forecasting in terrain-following coordinates: Formulation and skill assessment of the regional ocean modeling system. *Journal of Computational Physics*, *227*, 3595–3624.

Holbrook, N. J., Goodwin, I. D., McGregor, S., Molina, E., & Power, S. B. (2011). ENSO to multi-decadal time scale changes in East Australian Current transports and Fort Denison sea level: Oceanic Rossby waves as the connecting mechanism. *Deep Sea Research Part II: Topical Studies in Oceanography*, *58*(5), 547–558. https://doi.org/10.1016/j.dsr2.2010.06.007

Hu, D., L., Wu, W., Cai, A. S., Gupta, A., Ganachaud, B., Qiu, A. L., et al. (2015). Pacific western boundary currents and their roles in climate. *Nature*, *522*, 299–308. https://doi.org/10.1038/nature14504.

Kessler, W. S., & Cravatte, S. (2013). Mean circulation of the Coral Sea. *Journal of Geophysical Research: Oceans*, *118*, 6385–6410. https://doi.org/10.1002/2013JC009117

Lambert, E., Le Bars, D., & de Ruijter, W. P. M. (2016). The connection of the Indonesian Throughflow, South Indian Ocean Countercurrent and the Leeuwin Current. *Ocean Science*, *12*, 771–780. https://doi.org/10.5194/os-12-771

Li, H., Xu, F., Zhou, W., Wang, D., Wright, J. S., Liu, Z., et al. (2017). Development of a global gridded Argo data set with Barnes successive corrections. *Journal of Geophysical Research: Oceans*, *122*, 866–889. https://doi.org/10.1002/2016JC012285

Mata, M., Tomczak, M., Wijffels, S. E., & John, A. C. (2000). East Australian Current volume transports at 30S: Estimates from the World Ocean Circulation Experiment hydrographic sections PR11/P6 and the PCM3 current meter array. *Journal of Geophysical Research*, *105*, 28509–28526.

Menezes, V. V., Phillips, H. E., Schiller, A., Bindoff, N. L., Domingues, C. M., & Vianna, M. L. (2014). South Indian Countercurrent and associated fronts. *Journal of Geophysical Research: Oceans*, *119*, 6763–6791. https://doi.org/10.1002/2014JC010076

Menezes, V. V., Phillips, H. E., Schiller, A., Domingues, C. M., & Bindoff, N. L. (2013). Salinity dominance on the Indian Ocean Eastern Gyral Current. *Geophysical Research Letters*, *40*, 5716–5721. https://doi.org/10.1002/2013GL057887

Menezes, V. V., Phillips, H. E., Vianna, M. L., & Bindoff, N. L. (2016). Interannual variability of the South Indian Countercurrent. *Journal of Geophysical Research: Oceans*, *121*, 3465–3487. https://doi.org/10.1002/2015JC011417

Metzger, E. J., Hurlburt, H. E., Xu, X., Shriver, J. F., Gordon, A. L., Sprintall, J., et al. (2010). Simulated and observed circulation in the Indonesian Seas: 1/12° global HYCOM and the INSTANT observations. *Dynamics of Atmospheres and Oceans*, *50*, 275–300.

Meuleners, M. J., Pattiaratchi, C. B., & Ivey, G. N. (2007). Numerical modeling of the mean flow characteristics of the Leeuwin Current System. *Deep Sea Research, Part II: Topical Studies in Oceanography*, *54*, 837–858. https://doi.org/10.1016/j.dsr2.2007.02.003

Meyers, G., Bailey, R. J., & Worby, A. P. (1995). Geostrophic transport of Indonesian Throughflow. *Deep Sea Research, Part I: Oceanographic Research Papers*, *42*, 1163–1174.

Middleton, J. F., Arthur, C., Van Ruth, P. D., Ward, T. M., McClean, J. L., Maltrud, M. E., et al. (2007). El Nin∼o effects and upwelling off South Australia. *Journal of Physical Oceanography*, *37*, 2458–2477.

Middleton, J. F., & Bye, J. A. T. (2007). A review of the shelf-slope circulation along Australia's southern shelves: Cape Leeuwin to Portland. *Progress in Oceanography*, *75*, 1–41.

Middleton, J. F., & Cirano, M. (2002). A northern boundary current along Australia's southern shelves: The Flinders Current. *Journal of Geophysical Research*, *107*(C9), 3129.

Oke, P. R., & Schiller, A. (2007). Impact of Argo, SST and altimeter data on an eddy-resolving ocean reanalysis. *Geophysical Research Letters*, *34*, L19601. https://doi.org/10.1029/2007GL031549

Palastanga, V., van Leeuwen, P., Schouten, M., & de Ruijter, W. (2007). Flow structure and variability in the subtropical Indian Ocean: Instability of the South Indian Ocean Countercurrent. *Journal of Geophysical Research*, *112*, C01001. https://doi.org/10.1029/2005JC003395

Pattiaratchi, C., & Woo, M. (2009). The mean state of the Leeuwin Current system between North West Cape and Cape Leeuwin. *Journal Royal Society Western Australia*, *92*, 221–241.

Pattiaratchi, C. B. (2011). Coastal tide gauge observations: Dynamic processes present in the Fremantle record. In A. Schiller & G. B. Brassington (Eds.), *Operational oceanography in the 21st century* (pp. 185–202). Dordrecht, the Netherlands: Springer.

Pattiaratchi, C. B., & Buchan, S. (1991). Implications of long-term climate change for the Leeuwin Current. *Journal Royal Society Western Australia*, *74*, 133–140.

Potemra, J. T. (2005). Indonesian Throughflow transport variability estimated from satellite altimetry. *Oceanography*, *18*, 94–103.

Ridgway, K. R. (2007). Seasonal circulation around Tasmania: An interface between eastern and western boundary dynamics. *Journal of Geophysical Research*, *112*, C10016. https://doi.org/10.1029/2006JC003898

Ridgway, K. R., Coleman, R., Bailey, R., & Sutton, P. (2008). Decadal variability of East Australian Current transport inferred from repeated high-density XBT transects: A CTD survey and satellite altimetry. *Journal of Geophysical Research*, *113*, C08039. https://doi.org/10.1029/2007JC004664

Ridgway, K. R., & Condie, S. A. (2004). The 5500-km-long boundary flow off western and southern Australia. *Journal of Geophysical Research*, *109*, C04017. https://doi.org/10.1029/2003JC001921

Ridgway, K. R., & Dunn, J. R. (2003). Mesoscale structure of the mean East Australian Current system and its relationship with topography. *Progress in Oceanography*, *56*, 189–222.

Ridgway, K. R., & Dunn, J. R. (2007). Observational evidence for a Southern Hemisphere oceanic supergyre. *Geophysical Research Letters*, *34*, L13612. https://doi.org/10.1029/2007GL030392

Ridgway, K. R., & Godfrey, J. S. (1994). Mass and heat budgets in the East Australian Current: A direct approach. *Journal of Geophysical Research*, *99*, 3231–3248.

Ridgway, K. R., & Godfrey, J. S. (1997). Seasonal cycle of the East Australian Current. *Journal of Geophysical Research*, *102*, 22,921–22,936.

Ridgway, K. R., & Godfrey, J. S. (2015). The source of the Leeuwin Current seasonality. *Journal of Geophysical Research: Oceans*, *120*, 6843–6864. https://doi.org/10.1002/2015JC011049

Rintoul, S. R., & Sokolov, S. (2001). Baroclinic transport variability of the Antarctic Circumpolar Current south of Australia (WOCE repeat section SR3). *Journal of Geophysical Research*, *106*, 2815– 2832.

Roemmich, D., & Gilson, J. (2009). The 2004–2008 mean and annual cycle of temperature, salinity, and steric height in the global ocean from Argo program. *Progress in Oceanography*, *82*, 81–100.

Rosell-Fieschi, M., Rintoul, S. R., Gourrion, J., & Pelegrí, J. L. (2013). Tasman Leakage of intermediate waters as inferred from Argo floats. *Geophysical Research Letters*, *40*, 5456–5460. https://doi.org/10.1002/2013GL057797

Schiller, A. (2012). Ocean circulation on the North Australian Shelf. *Continental Shelf Research*, *31*, 1087–1095.

Schiller, A., Oke, P. R., Brassington, G. B., Entel, M., Fiedler, R., Griffin, D. A., et al. (2008). Eddy-resolving ocean circulation in the Asian-Australian region inferred from an ocean reanalysis effort. *Progress in Oceanography*, *76*, 334–365.

Sen Gupta, A., McGregor, S., van Sebille, E., Ganachaud, A., Brown, J. N., & Santoso, A. (2016). Future changes to the Indonesian Throughflow and Pacific circulation: The differing role of wind and deep circulation changes. *Geophysical Research Letters*, *43*, 1669–1678. https://doi.org/10.1002/2016GL067757

Sikiric, M., Janekovic, I., & Kuzmic, M. (2009). A new approach to bathymetry smoothing in sigma-coordinate ocean models. *Ocean Modelling*, *29*(2), 128–136.

Sloyan, B. M., Ridgway, K. R., & Cowley, R. (2016). The East Australian current and property Transport at 27S from 2012–2013. *Journal of Physical Oceanography*, *46*, 993–1008.

Smith, R. L., Huyer, A., Godfrey, J. S., & Church, J. (1991). The Leeuwin current off western Australia, 1986–1987. *Journal Physical Oceanography*, *21*, 323–345.

Speich, S., Blanke, B., de Vries, P., Drijfhout, S., Doos, K., Ganachaud, A., & Marsh, R. (2002). Tasman leakage: A new route in the global ocean conveyor belt. *Geophysical Research Letters*, *29*(10), 1416. https://doi.org/10.1029/ 2001GL014586

Sprintall, J., & Revelard, A. (2014). The Indonesian throughflow response to Indo-Pacific climate variability. *Journal of Geophysical Research: Oceans*, *119*, 1161–1175. https://doi.org/10.1002/2013JC009533

Sprintall, J., Wijffels, S. E., Molcard, R., & Jaya, I. (2009). Direct estimates of the Indonesian throughflow entering the Indian Ocean: 2004–2006. *Journal of Geophysical Research*, *114*, C07001. https://doi.org/10.1029/2008JC005257

Susanto, R. D., Ffield, A., Gordon, A. L., & Adi, T. R. (2012). Variability of Indonesian Throughflow within Makassar Strait, 2004–2009. *Journal of Geophysical Research*, *117*, C09013. https://doi.org/10.1029/2012JC008096

Susanto, R. D., & Song, Y. T. (2015). Indonesian Throughflow proxy from satellite altimeters and gravimeters. *Journal of Geophysical Research: Oceans*, *120*, 2844–2855. https://doi.org/10.1002/2014JC010382

Suthers, I. M., Everett, J. D., Roughan, M., Young, J. W., Oke, P. R., Condie, S. A., et al. (2011). The strengthening East Australian Current, its eddies and biological effects-An introduction and overview. *Deep-sea Research*. *Part II, Topical Studies in Oceanography*, *58*, 538–546.

van Sebille, E., England, M. H., Zika, J. D., & Sloyan, B. M. (2012). Tasman leakage in a fine resolution ocean model. *Geophysical Research Letters*, *39*, L06601. https://doi.org/10.1029/2012GL051004

Waite, A. M., Thompson, P. A., Pesant, S., Feng, M., Beckley, L. E., Domingues, C. M., et al. (2007). The Leeuwin Current and its eddies: An introductory overview. *Deep Sea Research II: Topical Studies in Oceanography*, *54*, 789–796.

Wang, Q., Danilov, S., Hellmer, H., Sidorenko, D., Schröter, J., & Jung, T. (2013). Enhanced cross-shelf exchange by tides in the western Ross Sea. *Geophysical Research Letters*, *40*, 5735–5739. https://doi.org/10.1002/2013GL058207

Webster, M. A., & Petkovic, P. (2005). *Australian bathymetry and topography grid, June 2005* (Vol. 2005/12, 30 pp.). Geoscience Australia Record.

Weijer, W., Sloyan, B. M., Maltrud, M. E., Jeffery, N., Hecht, M. W., Hartin, C. A. (2012). The Southern Ocean and its Climate in CCSM4. *Journal of Climate*, 25, 2652–2675.

Wijeratne, E. M. S., Pattiaratchi, C., Haigh, I. D., & Eliot, M. (2012). *The seasonal cycle of sea level around Australia*. Paper presented at Australian Coastal and Ocean Modelling and Observations Workshop (ACOMO), At Canberra, Australia, https://doi.org/10.13140/2.1.2613.0889

Woo, M., & Pattiaratchi, C. B. (2008). Hydrography and waters masses off the Western Australian coast. *Deep Sea Research Part I: Oceanographic Research Papers*, *55*, 1090–1104.

Yit Sen Bull, C., & van Sebille, E. (2016). Sources, fate, and pathways of Leeuwin Current water in the Indian Ocean and Great Australian Bight: A Lagrangian study in an eddy-resolving ocean model. *Journal of Geophysical Research: Oceans*, *121*, 1626–1639. https://doi.org/10.1002/2015JC011486

Zilberman, N. V., Roemmich, D. H., & Gille, S. T. (2014). Meridional volume transport in the South Pacific: Mean and SAM-related variability. *Journal of Geophysical Research: Oceans*, *119*, 2658–2678. https://doi.org/10.1002/2013JC009688